

# **SATELLITE DRAG VALIDATION OF THE THERMOSPHERE-IONOSPHERE ELECTRODYNAMICS GENERAL CIRCULATION MODEL**

**Chin S. Lin, et al.**

**Boston College  
140 Commonwealth Ave  
Chestnut Hill, MA 02467**

**29 February 2013**

**Technical Memorandum**

**APPROVED FOR PUBLIC RELEASE; DISTRIBUTION IS UNLIMITED.**



**AIR FORCE RESEARCH LABORATORY  
Space Vehicles Directorate  
3550 Aberdeen Ave SE  
AIR FORCE MATERIEL COMMAND  
KIRTLAND AIR FORCE BASE, NM 87117-5776**

## **DTIC COPY**

### **NOTICE AND SIGNATURE PAGE**

Using Government drawings, specifications, or other data included in this document for any purpose other than Government procurement does not in any way obligate the U.S. Government. The fact that the Government formulated or supplied the drawings, specifications, or other data does not license the holder or any other person or corporation; or convey any rights or permission to manufacture, use, or sell any patented invention that may relate to them.

This report was cleared for public release by the 377 ABW Public Affairs Office and is available to the general public, including foreign nationals. Copies may be obtained from the Defense Technical Information Center (DTIC) (<http://www.dtic.mil>).

AFRL-RV-PS-TM-2013-0002 HAS BEEN REVIEWED AND IS APPROVED FOR PUBLICATION IN ACCORDANCE WITH ASSIGNED DISTRIBUTION STATEMENT.

//SIGNED//

---

Daniel M. Ober, DR-III, DAF  
Deputy Chief, Space Plasma Disturbance  
Specification & Forecast Section

//SIGNED//

---

Edward J. Masterson, Colonel, USAF  
Chief, Battlespace Environment Division

This report is published in the interest of scientific and technical information exchange, and its publication does not constitute the Government's approval or disapproval of its ideas or findings.

REPORT DOCUMENTATION PAGE			Form Approved OMB No. 0704-0188	
Public reporting burden for this collection of information is estimated to average 1 hour per response, including the time for reviewing instructions, searching existing data sources, gathering and maintaining the data needed, and completing and reviewing this collection of information. Send comments regarding this burden estimate or any other aspect of this collection of information, including suggestions for reducing this burden to Department of Defense, Washington Headquarters Services, Directorate for Information Operations and Reports (0704-0188), 1215 Jefferson Davis Highway, Suite 1204, Arlington, VA 22202-4302. Respondents should be aware that notwithstanding any other provision of law, no person shall be subject to any penalty for failing to comply with a collection of information if it does not display a currently valid OMB control number. <b>PLEASE DO NOT RETURN YOUR FORM TO THE ABOVE ADDRESS.</b>				
<b>1. REPORT DATE (DD-MM-YYYY)</b> 07-02-2013		<b>2. REPORT TYPE</b> Technical Memorandum		<b>3. DATES COVERED (From - To)</b> 18 Jul 2012 – 01 Feb 2013
<b>4. TITLE AND SUBTITLE</b> Satellite Drag Validation of the Thermosphere-Ionosphere Electrodynamics General Circulation Model			<b>5a. CONTRACT NUMBER</b> FA9453-12-C-0205	
			<b>5b. GRANT NUMBER</b>	
			<b>5c. PROGRAM ELEMENT NUMBER</b> 62601F	
<b>6. AUTHOR(S)</b> C. S. Lin, S. B. Cable, E. K. Sutton, F. A. Marcos, J. M. Retterer, and S. H. Delay			<b>5d. PROJECT NUMBER</b> 1010	
			<b>5e. TASK NUMBER</b> PPM00014330	
			<b>5f. WORK UNIT NUMBER</b> EF008140	
<b>7. PERFORMING ORGANIZATION NAME(S) AND ADDRESS(ES)</b> Boston College 140 Commonwealth Ave Chestnut Hill, MA 02467			<b>8. PERFORMING ORGANIZATION REPORT NUMBER</b>	
<b>9. SPONSORING / MONITORING AGENCY NAME(S) AND ADDRESS(ES)</b> Air Force Research Laboratory Space Vehicles Directorate 3550 Aberdeen Avenue SE Kirtland AFB, NM 87117-5776			<b>10. SPONSOR/MONITOR'S ACRONYM(S)</b> AFRL/RVBXP	
			<b>11. SPONSOR/MONITOR'S REPORT NUMBER(S)</b> AFRL-RV-PS-TM-2013-0002	
<b>12. DISTRIBUTION / AVAILABILITY STATEMENT</b> Approved for public release; distribution is unlimited. (377ABW-2013-0130 dtd 5 Feb 2013 )				
<b>13. SUPPLEMENTARY NOTES</b> Contract associated with in-house effort EF008140.				
<b>14. ABSTRACT</b> Orbital drag errors impact many Air Force missions including predicting re-entry times and locations, collision avoidance warnings and maintenance of the world's best catalog of all space objects. The empirical operational satellite drag models have had persisting deficiencies in their orbit predictions. The potential of physics based models for more accurate space weather predictions is currently under intense scientific investigation. Model development efforts require appropriate validation efforts. We evaluate key attributes of the Thermosphere-Ionosphere Electrodynamics General Circulation Model (TIEGCM) developed by the National Center for Atmospheric Research. This validation uses accelerometer neutral density data from the CHAMP and GRACE satellites near 400 km and 500 km altitude respectively and the historic Air Force SETA data near 200 km altitude. Key physics improvement areas needed for a next generation satellite drag modeling are elucidated by evaluating model performance relative to thermosphere variability due to solar cycle, day of year and geomagnetic activity. Data assimilation is shown to be an effective mechanism for improving model specification and forecast accuracy.				
<b>15. SUBJECT TERMS</b> Satellite drag, Thermosphere Neutral Density, General Circulation Model, TIEGCM				
<b>16. SECURITY CLASSIFICATION OF:</b>			<b>17. LIMITATION OF ABSTRACT</b>  Unlimited	<b>18. NUMBER OF PAGES</b>  60
<b>a. REPORT</b> Unclassified	<b>b. ABSTRACT</b> Unclassified	<b>c. THIS PAGE</b> Unclassified		
				<b>19b. TELEPHONE NUMBER (include area code)</b>

This page is intentionally left blank.

## 1. Introduction

### a. Objective

AFRL has the mission of transitioning a next generation First Principles Predictive Assimilative Operational Satellite Drag Model to Air Force Space Command. This Tech Memo provides an initial assessment of the Thermosphere-Ionosphere Electrodynamics General Circulation Model (TIEGCM) with selected supporting scientific research noted as needed to place the results in context; it is not intended as a comprehensive review paper. Validation is done with satellite accelerometer neutral density data from the CHAMP (~400 km), GRACE (~500 km) and historic Air Force SETA (~200 km) missions. Aspects of TIEGCM Version 1.91 studied are solar cycle, day of year and geomagnetic storm variations. Also described are assimilative techniques being implemented for the latest TIEGCM model, version 1.9.4. We identify key physics improvement areas for next generation First Principles Forecast operational satellite drag modeling to successfully upgrade current and future satellite orbital and reentry predictions.

### b. Relevance

Accurate specification and prediction of the space environment is necessary to calculate satellite drag and orbital trajectories precisely to support Air Force Space Command (AFSPC) in several areas including: (1) satellite reentry predictions, (2) timely Collision Avoidance warnings needed to protect International Space Station and other space assets from being hit by debris and other space objects and to minimize the need for maneuvers and (3) catalog maintenance for precision orbit determination of all space objects. The AFSPC present stated operational goal is a 3-day satellite density forecast with error of 5% for altitudes 90 to 500 km. As a more quantitative requirement, Anderson, et al., 2009 state that the 24 hour orbit prediction errors of significance include 250 meters at 200 km and 100 meters at 400 km. Aerodynamic drag depends on neutral density  $\rho$ , as well as area-to-mass ratio  $A/m$ , drag coefficient  $C_D$  and velocity  $V$  (includes atmosphere rotation with earth plus residual winds) respectively:

$$a_D = -\frac{1}{2} \left( \frac{C_D A}{m} \right) \rho V^2 \quad (1)$$

Neutral mass density variations are recognized as the primary cause of orbital drag errors. While specific knowledge of the reentering vehicle's area/mass ratio and drag coefficient (see e.g. Sutton, 2009; Sentman, 1961), as well as neutral wind fields, are also critical, we focus on the neutral density variations. Thermospheric density is driven mainly by the highly variable sun's electromagnetic radiation and interaction of solar particles with earth's magnetosphere. Upward propagating waves are also becoming identified as a significant contributor to many aspects of thermosphere variability. Thus meaningful progress on low Earth orbit trajectory forecasts requires significantly

improved knowledge of space weather and its effects of Earth's neutral upper atmosphere.

### c. Thermospheric Variability Drivers

The Earth's upper atmosphere is a strongly forced and coupled system driven mainly by the sun's solar EUV and solar wind interactions. Solar EUV is deposited mainly at low and middle latitudes. Geomagnetic storm inputs are significant at high latitudes. Upward propagating gravity waves and tides also contribute to thermosphere variability. For a review of fundamentals of thermosphere heating, see Roble, 1977.

Solar EUV is the main mechanism for heating Earth's thermosphere. EUV radiation, at wavelengths less than 200 nm typically accounts for about 75 - 80% of the energy input to the thermosphere, and thereby determines its basic structure. The neutral density varies by an order of magnitude at 400 km due to the solar variability of the EUV flux. Below about 80 km atmospheric air is mainly molecular (~ 78.08% molecular nitrogen, 20.95% molecular oxygen and 0.93% argon, with trace gases including 0.038% carbon dioxide and 0.0005% helium). These gases are mixed such that the composition is relatively constant up to about 80 km. Above 80 km atomic species result from photodissociation and chemical reactions due to solar EUV radiation. At higher altitudes the different species are separated gravitationally such that the main thermospheric constituent is generally atomic oxygen from about 200 - 600 km. Helium densities compete with atomic oxygen above about 600 km during low solar flux conditions.

Solar EUV fluxes originate in the chromosphere, chromosphere-corona transition region and corona. In contrast to visible radiation (i.e. resulting in the "solar constant"), EUV emissions are highly variable, with chromospheric emissions changing by a factor of 2 or more and coronal emissions varying by a factor of 50-150 over the solar cycle. The thermosphere response to solar activity consequently varies with the solar cycle, the 27 day solar rotation period, with day-to-day changes superimposed. The density can change by an order of magnitude at 400 km over a solar cycle. At 200 km the solar cycle variability is ~ a factor of 3. Solar EUV energy is deposited mainly at low to mid-latitudes, in the vicinity of the sub solar point. Since this heating creates a pressure bulge that drives winds to transport heat away from the hot dayside toward the Earth's cold nightside, temperatures on the dayside are only ~30% higher than those on the nightside. Even if the Earth did not rotate, solar heating would still reach the nightside and affect density there.

Geomagnetic storms account on average for about 20% of the thermospheric heating. These storm occurrences are, however, episodic and unpredictable. They are a result of solar wind energy transferred to the thermosphere mainly at high latitudes. The solar wind is a supersonic plasma that carries with it the magnetic field of the Sun. Interaction of the solar wind with Earth's magnetic field results in auroral particle precipitation and frictional dissipation of ionospheric current systems. If the field direction in the solar wind is opposite to that of the Earth's dipole magnetic field then subsequent interactions allow for significant amounts of mass, momentum and energy to

be transferred into the magnetosphere. These conditions usually result in magnetic storms that produce strong auroral particle bombardment and strong electric currents which close in the ionosphere and drive rapid upper-atmospheric motions. During geomagnetic storms, the disturbed solar wind compresses the Earth's magnetosphere. Intense field-aligned currents couple the auroral ionosphere with the magnetosphere extracting electromagnetic energy (Poynting flux) that heats both the ionized and neutral gases. Joule heating heats the neutral atmosphere in the altitude region at about 120-150 km, drives horizontal winds, and forces upwelling of the neutral atmosphere. Intense electric fields in the high-latitude ionosphere drive rapid plasma convection that couple via collisions with neutral winds. At the same time, the auroral oval expands and energetic particles precipitating into the lower thermosphere enhance ionospheric conductivities. The rate of electromagnetic energy input at high latitudes can rise to more than ten times greater than that of the global EUV. The resulting heat and momentum input produces very large and abrupt changes in neutral density and local neutral composition, generates traveling gravity waves and excites strong winds. The heavier molecules  $N_2$  and  $O_2$ , abundant in the lower thermosphere, are transported to higher altitudes. Thus, a global circulation system is set up to redistribute mass, momentum, and energy (Fuller-Rowell, et al., 1996). Localized energy input is spread globally with complex temporal and spatial variability.

Figure 1 is a simplified schematic sketch of the system to be simulated by models, showing the relative roles of high latitude solar wind heating; low latitude solar EUV and upward waves in various latitude regions (Forbes, 2007). Figure 2 (taken from Knipp, et al., 2005) illustrates the relative significance of solar and auroral forcings from 1975 to 2005. Solar power (grey line) generally dominates but episodic joule power during geomagnetic storms can exceed the global EUV input. Forcing due to particle precipitation (grey dots) is relatively small. The time and space variation of neutral atmosphere density consequently is sensitive to solar and geomagnetic activity as well as to upward propagating waves. Most thermospheric variability comes from variability of its driving sources over periods ranging from part of a day to a solar cycle. During geomagnetic storms especially, the thermosphere can vary rapidly and irregularly over very short time periods.

A long-recognized generally less significant energy source, tidal and gravity waves propagating up from the lower atmosphere, further modulates the thermosphere. Recent analyses have shown that upward propagating effects originating from tropospheric heating processes that reflect land-sea distributions, topography, and other factors can potentially explain several phenomena including longitudinal density variations observed in satellite density measurements (e.g. Forbes, et al., 2009) and possibly the semiannual variation (Akmaev, 2011).

#### d. Toward Next Generation Satellite Drag Models

Empirical models are particularly limited in their capability to respond to the highly variable solar and geomagnetic variations. They are parameterized in terms of mainly proxy geophysical indices that are daily, 3-hourly, and hourly at their highest resolution,

and so are not suited to track hour-to-hour variations. Further, being based on data, they are limited when extrapolating beyond the range of data. For example, the Jacchia-Bowman 2008 (JB08) operational model errors for large storms are ~27% for point measurements (Bowman, et al., 2008). Using orbit averages for selected storms showed that the smoothing reduced errors to ~13%. The recent solar minimum has shown errors of 50% because the F10 – EUV one-to-one relation did not hold. JB08, while using measurements as part of the EUV input, is still heavily weighted in favor of the F10 index. In fact the model has an ad hoc correction that arbitrarily represents density variability with decreasing solar flux in order to better match data.

The scientific and operational communities have recognized that significant improvements will require a shift away from empirical models currently used to physical models. Thus, next generation models of upper atmospheric density forecasts will necessarily be based on the physics of solar behavior and solar terrestrial interactions. Large scale computer simulations of thermosphere circulation are demonstrating their ability to provide global distribution of the mass density temperature and winds. These complex physical models hold promise of great progress in forecasting long term space weather variations. While the climatological variation of the global or orbit-averaged density is relatively well captured by these models, describing regional density structures and short-term density variations is significantly more challenging. The observational solar data sets and underlying subtle physics needed to achieve the potential accuracy of these models are becoming available. The satellite drag community recognizes the future impact of these models vs the simpler empirical models driven by proxy indicators of solar heating.

Physical modeling is of course now the basis for our improved terrestrial weather forecasts. The models are based on a set of “first principles” equations used to predict future state of the atmosphere: equations of continuity, conservation of energy, momentum and the ideal gas law are used to evolve the thermospheric parameters neutral density, temperature winds and composition. Their use is obviously not straightforward in the empirical modeling sense of simple analytical functions. The nonlinear partial differential equations are necessarily solved by numerical methods to obtain approximate solutions. Weather forecast models also have the benefit of a huge amount of input data from land, sea, air and space-based sensors and a very long period for upgrading. Analogously, space weather physical models use the same basic equations to produce space environment parameter predictions at given location. As noted in Section 1c, the upper atmosphere is strongly affected by variable high energy electromagnetic radiation ultraviolet from the Sun, as well as by bombardment from energetic auroral electrons and by electric current flowing from the magnetosphere. It is also influenced by atmospheric waves that propagate up from lower levels. Unlike the lower atmosphere, the upper atmosphere is heterogeneous, with diatomic nitrogen and oxygen giving way to monatomic oxygen at the higher levels. Also unlike the lower atmosphere, the dynamics is strongly influenced by molecular viscosity, heat conduction, and diffusion, as well as by the force exerted by the electric current flowing through the Earth's magnetic field. Strong external forcing and relatively rapid dissipative processes mean that the model cannot run freely for long simulated times without updates to the inputs, unlike lower-



atmospheric weather and climate models. Also unlike lower atmosphere models, data-assimilation techniques are challenged by sparse thermosphere and heat input data.

In this Tech Memo we review pertinent aspects of neutral density validation for the NCAR TIEGCM (Thermosphere–Ionosphere Electrodynamics General Circulation Model). This TM uses Version 1.91 of the TIEGCM. Primary references for the historical development of this model are Dickinson, et al., 1981, 1984) Roble and Ridley, 1987, 1994, Roble, et al., 1987, 1988, and Richmond, et al., 1992. Another excellent summary tracing the model development to its current version 1.9.4 is given by Solomon, et al., 2012. The model description below is directly from NCAR’s website at <http://www.hao.ucar.edu/modeling/tgcm/>:

“The NCAR Thermosphere-Ionosphere- Electrodynamics General Circulation Model (TIE-GCM) is a comprehensive, first-principles, three-dimensional, non-linear representation of the coupled thermosphere and ionosphere system that includes a self-consistent solution of the low-latitude electric field. The model solves the three-dimensional momentum, energy and continuity equations for neutral and ion species at each time step, using a semi-implicit, fourth-order, centered finite difference scheme, on each pressure surface in a staggered vertical grid. It has 29 constant-pressure levels in the vertical, extending from approximately 97 km to 500 km in intervals of one-half scale height, and a 5° x 5° latitude-longitude grid, in its base configuration. The time step is 120 s.”

“Hydrostatic equilibrium, constant gravity, steady-state ion and electron energy equations, and incompressibility on a constant pressure surface, are assumed. Ion velocities are derived from the potential field created by combining the imposed magnetospheric potential with the low-latitude dynamo potential, and then calculating ion velocities from ExB drifts, rather than solving the ion momentum equations explicitly. Some minor species are not currently included in the model, including hydrogen and helium and their ions, and argon. Several parameterizations are used in the TIE-GCM: an empirical model is used to specify photoelectron heating; the production of secondary electrons is included using an empirical model derived from two-stream calculations, the effects of mixing by gravity waves are included using an eddy diffusion formulation; CO<sub>2</sub> is included by specifying a lower boundary condition and assuming that it is in diffusive equilibrium. The upper boundary conditions for electron heat transfer and electron number flux are empirical formulations. At the lower boundary, atmospheric tides are specified using the Global Scale Wave Model (GSWM).”

AFRL has the responsibility of Technology Transitioning to AFSPC an operational physical satellite drag model. Figure 3 shows a block diagram of an assimilative TIEGCM. In practice, an operational physical model uses space-based measurements of actual solar EUV and high latitude heating inputs plus tides from below as well as thermosphere and ionosphere data, all augmented by data assimilation techniques. This effort is also supported by the five-year, \$1.5M/year AFOSR funded MURI with the University of Colorado. This effort completed in 2012 significantly advanced understanding of the satellite drag environment to enable specification and prediction at

the “next level” of performance. The MURI states “ The scope of this MURI topic is the elucidation of those physical concepts and predictable key indicators of energy inputs to the atmosphere that will update and calibrate current operational satellite drag models and lead to the accurate prediction of thermospheric densities and, hence, a precise prediction of the locations of satellites.” Achieving an eventual 5% forecast capability requires (1) accurate description and forecasts of relevant heat and dynamics inputs (2) a model that accurately represents the thermosphere response to the external heating and (3) physical characteristics of the spacecraft object used in orbit propagators. Figure 4 shows how the various areas of study under the MURI support the capability for AFRL to transition the needed Precision Orbit Determination.

#### e. Memo Overview

This memo summarizes the initiation of detailed evaluation of physical satellite drag models to support implementation of next-generation satellite drag forecast capabilities. Section 2 briefly describes the CHAMP, GRACE and SETA accelerometer experiments that provided neutral density data used in this TM. Sections 3, 4 and 5 illustrate TIEGCM response to variations with day of year (semiannual), solar cycle and geomagnetic storms respectively. Implementation of data assimilation techniques are noted in section 6. A statistical summary of results and preliminary comparison to empirical modeling is in Section 7. A summary is given in Section 8.

## **2. Data Sources**

CHAMP, launched 15 July 2000 into a near circular, near polar (inclination angle  $87^\circ$ ) orbit with an initial altitude of about 450 km, provided unprecedented new high-resolution neutral density data until near its reentry on 19 Sept 2011. The GRACE mission, using two satellites separated by a nominal 220 km, was launched 17 March 2002 into an 89-degree inclination orbit with an initial perigee near 500 km, and is still operational. CHAMP uses the STAR (Spatial Triaxial Accelerometer for Research) accelerometer built by ONERA, France (Bruinsma, et al., 2004). GRACE, at higher altitude, uses SuperSTAR, a more sensitive version of STAR (Tapley, et al., 2004). Density is determined from accelerometers aboard these two gravity mission satellites by directly measuring decelerations due to aerodynamic drag. Neutral density is derived from these drag measurements according to Eq (1) using knowledge of the satellite’s area-to-mass ratio, drag coefficient and velocity. Data processing to extract neutral density (and winds) from these accelerometers is given in Sutton, et al., 2007.

The Satellite Electrostatic Triaxial Accelerometer instruments were flown on three satellites in near-circular, sun-synchronous orbit (1030/2230 hours) with an altitude range between 170 and 240 km. A description of the SETA instrument and data processing to derive density and winds is given by Marcos and Forbes, 1985 and references therein. Additional results from the SETA flights were journal published between 1985 and 2000 (see e.g. Rhoden, et al., 2000 and references therein). Figure 5 summarizes the satellite orbit properties. The satellite altitude is below 200 km over most of the northern

hemisphere dayside conditions throughout each mission. We utilize data at latitudes +/- 83.7 degrees from the SETA 2 (May-November, 1982).

Data are presented as measured and model densities normalized to a constant altitude of 400 km for CHAMP and GRACE and to 200 km for SETA, respectively. In both cases normalization is carried out using NRLMSIS (appropriate to the solar-geophysical conditions for the measurement). For example the normalized CHAMP density at 400 km is calculated as  $\text{CHAMP (400 km)} = \text{CHAMP (at altitude } z) \times \frac{\text{MSIS (400km)}}{\text{MSIS (altitude } z)}$ . The effect of this normalization model is small, particularly compared to the spatial-temporal variability of the density features under study. In addition ratio of measured densities to TIEGCM simulations is presented.

### **3. The Semiannual Variation**

The most prominent feature of thermospheric day to day structure (other than solar/geomagnetic variations) is the so-called semiannual variation (hereafter SAV) characterized by maxima near equinoxes and minima near solstices. It was first observed in satellite drag data by Paetzold and Zschorner, 1961. Additional studies revealed that the magnitude of the annual minimum to maximum variation is solar cycle dependent (Bowman, et al., 2008) and can be more than 100%. The maximum yearly difference, from the yearly minimum to the yearly maximum, varies by as much as 60% from year to year, and the phases of the minima and maxima also can change by about a month from year to year. There are also latitude structures, hemispheric asymmetries (e.g. Hedin and Mayr, 1987), and interannual variations. Over 50 years since the SAV discovery, the physical mechanism is not clear. A full discussion is beyond the scope of this Memo (see Guo, et al., 2008; Lei, et al., 2012 for recent excellent reviews).

There was a possibility that the SAV was contained in existing physical models (Roble, private communication). However, Qian, et al., 2009 utilizing drag data from two satellites showed that the SAV was not contained in TIEGCM. Figure 6 (taken from Lin, et al., 2010) illustrates this model deficiency. The top part of the figure shows ratio of TIEGCM to density data derived from orbital drag on two different satellites. The bottom part of the figure shows ratio of TIEGCM to CHAMP accelerometer data during 2002. In both cases the model is too high particularly during the July minima. For CHAMP the difference is about a factor of two higher during July than at other times. Note that the data also showed that ratios of model to data are higher during nighttime than daytime; i.e. there is an apparent local time error in the model. This effect was also noted in the assimilation studies described in Section 6. Simulations indicate that seasonal effects in TIEGCM do not fully account for the observed annual/semiannual amplitude, primarily because of the lack of a minimum during northern hemisphere summer. Qian, et al., 2009 suggested incorporating a variable eddy diffusion coefficient larger during solstices than equinoxes, and stronger turbulence in summer than in winter tailored to match the orbital drag data from five satellites. TIEGCM version 1.91 utilizes a constant value. Lin, et al., 2010, using CHAMP data, also showed how a variable eddy diffusion coefficient, based on CHAMP data could allow TIEGCM to match the semiannual variation in CHAMP data. Their variable eddy diffusion coefficient is shown

to the left on Figure 7. Increased eddy diffusivity at solstices decrease model density and decreased eddy diffusivity at equinoxes will increase model density. As a result, the top right panel shows CHAMP (black curve) and TIEGCM (red curve) densities during 2002 now in good agreement, resulting in a ratio of model to data that is relatively flat (bottom right panel). All TIEGCM data were normalized by a factor of 1.15. Seasonally varying formulae of CHAMP equatorial eddy diffusivity with a systematic bias improves agreement between TIEGCM and CHAMP neutral density values. An ad hoc prescribed seasonally varying eddy diffusivity correction has been incorporated into version 1.9.4 of TIEGCM (Qian and Solomon, 2012). However, as was noted by Qian, et al., 2009, this isn't necessarily the correct or complete mechanism. Upward propagating gravity waves and tides may be involved. The seasonal dependence of gravity wave activity is known to peak around solstices, and minimize around equinoxes. Akmaev, et al., 2008 suggests gravity wave activity in the Whole Atmosphere Model (Akmaev, 2011) may account for SAV.

While semiannual variations are large, the changes occur over periods of months. Fitting the periodicity will minimize errors in forecasting satellite drag. Hedin and Mayr, 1987 in an analysis of wave structures in Dynamics Explorer data estimated that the upward propagating waves contributed about 5% to density errors at low latitudes. However, if the mechanism due to upward propagating effects has short term variations superimposed, as would be the case with disturbances originating below, then these will introduce errors into the density forecasts. Until the full mechanism is understood and a system exists for monitoring it, the SAV contribution to density errors remains to be resolved.

#### 4. Solar Cycle Variations

Annual average of densities normalized to 400 km densities were calculated over the period 2001-2009. For this study TIEGCM was driven by F10 as the solar EUV input. Note that annual solar flux varied from ~181 in 2001 to ~69 in 2008 and 2009. To focus on model performance without contributions due to large geomagnetic storms, data for  $a_p \leq 15$  were sorted according to LT 06-18 (Blue) and 18-06 hours (Red). Two mean values averaged over all latitudes were determined per orbit according to the equatorial LT. The half orbits are reasonably consistent with algorithms that compute orbit averaged data, and were also used in a preliminary examination of day-night differences. Statistical analyses over the solar cycle were computed based on the half orbit averages.

Plotted in Figure 8a are mean value ratios of TIEGCM/CHAMP sorted by LT bins and an average NRLMSIS/CHAMP (purple) with no LT bins. The TIEGCM/CHAMP ratio shows a local time difference with night ratios higher than day ratios by about 15% throughout the solar cycle. This effect was noted in the Section 3 above. The TIEGCM/CHAMP ratios are high at low solar flux, as expected, because densities are anomalously low during this unusual solar minimum (e.g. Emmert, et al., 2010). Since Figure 8a shows model to data, ratios are higher rather than lower. The EUV input is overestimated by the F10 index during this solar minimum so model values do not catch this anomaly. Empirical models, also driven by F10, clearly show similar behavior (see

the NRLMSIS /Drag curve). While part of this decreased neutral density could be unmodeled effect of thermospheric cooling related to anthropogenic gases, these would be of the order 20% (Emmert, et al., 2004; Marcos, et al., 2006). Figure 8a data show differences of order of 50%. Therefore the F10 index must be more significantly underestimating the actual EUV flux during this cycle, i.e. actual EUV flux during this cycle is lower than previous ones for the same F10 values (see Solomon, et al., 2010). Figure 8b shows relative standard deviations (std dev/mean) over the solar cycle. TIEGCM errors are generally higher on the nightside except for high solar flux (2002) conditions. TIEGCM errors are typically 5-7% higher than those of the empirical NRLMSIS model. As noted at the end of Section 3 this evaluation is based on version 1.91 of TIEGCM and therefore the error is increased due to the model's inaccurate semiannual variation. This shortcoming has been largely overcome in newer model versions; it is reasonable to assume that the TIEGCM and NRLMSIS errors are more comparable. An updated validation is recommended.

The limitations of using F10 have been understood since the earliest empirical models (Jacchia, 1964; Jacchia, 1970). Figure 8c (left side) shows solar irradiance vs wavelength and the non-black body EUV spectrum. Note that the F10 proxy is about 2 orders of magnitude off the right hand of the wavelength scale. The bottom half of this chart shows ratio of EUV lines as solar maximum to solar minimum. Some EUV lines vary by an order of magnitude over the solar cycle (Lean, 1997). F10BAR varies by about a factor of three over the solar cycle. Thus, real measurements are essential for capturing thermosphere response to solar electromagnetic energy input. TIEGCM can accept EUV and UV data. Even the original TGCM was developed to handle 57 EUV lines. While routine parameterization of Solar EUV Experiment (SEE) data as a physical model output is still in a research state (Dudock deWit, et al., 2009), preliminary studies of drag data from 2003 have demonstrated the benefit of realistic SEE inputs in TIEGCM to improve satellite drag specification (Qian, et al., 2008). Further analyses of drag data from 2002 through 2007 by Qian, et al., 2009 found that TIEGCM driven with measured solar irradiances does an excellent job in reproducing the densities forced by solar cycle, solar rotational, and geomagnetic variation. Solomon, et al., 2010 used SOHO and TIMED solar data to show that EUV levels were lower in 2008 than they were during the previous solar minimum; evidence that the unusually low level of EUV was primary cause of the observed low thermospheric density. Deng, et al., 2012 noting the anomalously low amount of geomagnetic activity in 2008 used TIEGCM simulations to find that the solar irradiance and geomagnetic energy variations account for 3/4 and 1/4 of the total neutral density decrease, respectively. With considerable research, more comprehensive solar EUV input-drag response relations will become achievable using new observational tools including the EVE experiment (Woods, et al., 2012) on Solar Dynamics Observatory plus abundant satellite drag and satellite accelerometer density data.

## 5. Geomagnetic Storm Response

### 5a. Section overview

Thermosphere response to geomagnetic conditions involves a series of complex and interrelated processes with high latitude solar wind deposition of energy being converted to global neutral density perturbations as noted in Section 1b. The serious shortcomings of present empirical models are most evident during large magnetic storms when these complex inputs and thermospheric responses become difficult to capture. Geomagnetic activity is recognized as the largest satellite drag uncertainty: AFSPC has shown that tracking errors at 400 km during even moderately disturbed periods are 65% greater than at quiet times. In this section we illustrate general features of TIEGCM's ability to represent the neutral density response to geomagnetic activity and use statistical evaluations to point out current capabilities and areas of improvement under investigation. We use the higher altitude CHAMP and GRACE data to demonstrate storm responses at high and low solar activity, then show SETA 1982 data to estimate TIEGCM capabilities in the reentry region. Figure 9 shows CHAMP (blue line) & GRACE (red line) perigee altitude vs time for 2001 through 2008 (top chart) with corresponding daily F10 solar flux values (bottom chart). Selected storm periods, noted by the vertical blue lines are in 2001-2 (F10~150 to >200 sfu) and 2007-2008 (F10 ~65 sfu). All storm periods are near November to reduce seasonal differences in the solar flux comparisons. For high solar flux there are two cases for CHAMP in 2001 with ap of 48 and 39 respectively and one in 2002 for CHAMP and GRACE with ap = 48. For solar minimum, there is one CHAMP-GRACE case in 2007 with ap = 56 and one in Nov 2008 with ap = 32.

### 5b. Storm Effects at High Altitudes During High Solar Flux

Figure 10 shows in geographic latitude-time coordinates: (a) CHAMP density response for two moderate storms in 2001 (FBAR ~214), (b) TIEGCM simulations of these storms and (c) ratio of CHAMP data to TIEGCM model. For the storm period starting Day 304; the top left side of Figure 10a shows the early evening hemisphere of the orbit (1924 hours) and the chart below it (Middle) gives the early morning side of the orbit (0724 hours). The normalized densities are obtained by first normalizing all CHAMP densities to 400 km altitude, then comparing storm period densities to a "quiet" condition determined from pre-storm density values vs latitude for the previous day where ap was low and fairly constant. The bottom charts show ap values for each case are similar: maximum ap= 48 on day 305 (left) and ap = 39 on day 358 (right). In both cases, the maximum density increase is at high latitudes (up to factor of two) for both local times and there is greater latitude penetration of storm enhancements on nightside. The response to the second storm starting on day 357 is much weaker (right side of Figure 10a), indicating possibly a local time dependence as well as the relatively imprecise correlation of heat input simulation vs actual drivers. The TIEGCM simulated response, Figure 10b, shows similar features but the response is weaker. Ratios of CHAMP 2001 densities to TIEGCM are shown in Figure 10c. The large amounts of blue on the chart indicate that the model has the relative responses fairly well represented

particularly early afternoon but with some underestimation for both storms at high latitude ~dawn/ and dusk where there are localized errors of a factor of two. The equatorial penetration is also under represented at night and early morning hours.

We next compare the response to a geomagnetic storm for both CHAMP and GRACE in Figure 11a. During the period studied, days 313-316 in 2002, CHAMP is in a 0917/2117 hours orbit (top left and right respectively) and GRACE is in an 0815/0615 orbit (bottom left and right respectively). Normalized density responses (as for Figure 10a) for this moderate storm during high solar flux conditions ( $F_{10.7} = 167$ ;  $a_p \text{ max} = 48$  on day 314) show similar features for CHAMP and GRACE. As for the CHAMP 2001 data in Figure 10, the maximum density increase is at high latitudes (up to factor of two) for all local times. Greater latitude penetration of storm enhancements occurs on nightside. Figure 11b, ratios of both CHAMP and GRACE to TIEGCM, show model simulations underestimate response to this storm, with the largest errors, up to a factor of two as for CHAMP in 2001, mainly confined to the high latitude winter hemisphere.

### 5c. Storm Effects at High Altitudes During Low Solar Flux

The response to a moderate storm in 2007 ( $F_{10.7}=68$ ,  $F_{10.7} = 72$ ) with  $a_p = 56$  on day 324 (20 Nov) is shown in Figure 12a for CHAMP (top left at 0826 hours and top right at 2026 hours) and GRACE below at 0123 hours (left) and 1323 hours (right). There are altitude and local time differences in the responses seen by the two satellites. As a general feature, at these low solar flux conditions, large density increases are up to factor of three (compared to  $\sim 2$  at high solar flux) during the approximately day long perturbation. The response at GRACE altitudes is overall stronger than that for CHAMP. This may be partly attributed to different composition effects. Thayer, et al., 2012 note the impact of Helium on geomagnetic response at GRACE altitude. TIEGCM does not include Helium. Corresponding simulated TIEGCM densities in Figure 12b show enhanced response in the northern (summer) hemisphere extending to all latitudes, but a weaker extension for CHAMP at 0826 hrs. Ratios of CHAMP and GRACE 2007 densities to TIEGCM (Figure 12c) show that the model again tends to underestimate responses at all latitudes and at all local times by as much as a factor of two.

The solar cycle response study above revealed a greater relative response magnitude at solar minimum attributed to similar energy absorbed by less mass (Burns, et al., 2004) and lower scale height and to increased disturbance with altitude due to lower scale heights during solar minimum. The disturbance region extension to all latitudes during solar min appears related to greater horizontal advection. Weaker EUV-driven pressure gradients result in stronger equatorward winds from Joule heating. Also, very low solar min density data imply weak summer-winter circulation, also enhancing summer hemisphere disturbance equatorward propagation. It is noted that the mean density is lower by around an order of magnitude so the satellite drag impact is not a significant operational problem.

Figure 13a shows CHAMP & GRACE normalized response to a small geomagnetic disturbance ( $a_p=32$ ) during days 312-315 of the deep 2008 solar minimum ( $F_{10.7}=69$ ;

FBAR =68). The satellites are in very similar local time orbits near roughly 1000/2300 hours. The responses are not readily interpreted: the maximum responses occur on the nightside for both satellites and are at low to middle latitudes. Further study is needed to unravel this low-mid latitude increase observed by both satellites. On the dayside, the response magnitude tends to favor northern latitudes. GRACE response is higher than that of CHAMP at lower latitudes. The relative response is again by a factor of three. The ratios of data to model (Figure 13b) are again up to a factor of two.

#### 5d. Storm Effects in Reentry Region

We next examine TIEGCM storm response in the reentry region. SETA data remain the only source of continuous full orbit accelerometer data in this region. As a case study, Figure 14a shows SETA-2 measured density normalized to an altitude of 200 km vs latitude and time during the August 1982 period with maximum ap of 179. The three frames are: dayside density (top), nightside density (middle) and geomagnetic indices ap and Dst (bottom). The dayside maximum response of ~65% occurs near 70 deg north latitude. In the south (winter) hemisphere the maximum response is ~30%, presumed due to reduced conductivity and hence reduced joule heating. The response penetrates to lower latitudes in the summer hemisphere due to prevailing summer to winter hemisphere winds. On the nightside penetration to low latitudes is about the same in both hemispheres due to auroral winds reinforced by day-night flow and reduced ion drag. Figure 14b, Top, gives the SETA response now normalized to pre-storm conditions and again showing maximum increase at high latitudes >50%. and greater latitude penetration of storm enhancements on nightside. Ratio of measured SETA data to TIEGCM (both at altitude) is on the bottom half of Figure 14c. Here, the ISEE-3 E-field data were available to drive the Weimer 2005 Model (REF). Dayside underestimates are generally ~10%; some high latitudes errors up to ~40%. Nightside typical errors are from ~30% up to 50%.

In Figure 15 we further examine this storm showing density and model data at three geographic latitudes (20, 60 and 70 deg) in the dayside northern (left) and southern (right) hemispheres. Empirical models densities are included for comparison. Measured density at 200 km (Y axis) has more structure than the JB08, J70, NRLMSIS and TIEGCM. All models underestimate the response at higher latitudes. For example, at 60 deg in the northern hemisphere, the ratio of density for day 219.5, approximately the maximum time of maximum response to this storm, to day 218, a quiet period, is 36% for SETA, 25% for NRLMSIS, 9% and 16% for TIEGCM.

### **6. Assimilation Techniques**

As was shown in Figures 3 and 4 data assimilation is a critical part of operational model development. The concept of dramatically reducing empirical model satellite orbit prediction errors by assimilating drag data, developed by AFRL (Marcos, et al., 1998), has been very successfully demonstrated in AFSPC's HASDM model (Storz, et al., 2002) and led to the MURI program. Prior to this, physical models of the thermosphere almost exclusively dealt with neutral composition and winds. Now they deal most heavily with satellite drag data. After



a transition period of several years, physical models with assimilation of large amounts of observations, are responsible for our local weather forecasting. Our next generation Space Weather forecasting is dependent on developing data assimilation techniques (Matsuo, et al., 2012 and references therein). Assimilative modeling provides a means to systematically identify and correct the inconsistencies between model specification and observations. For example, as shown in Section 5 above, today's models are capable of reproducing generic geomagnetic storm effects; modeling specific storms is challenging due to lack of accurate descriptions of the storm energy inputs. Assimilation of measurements into the modeling permits a means for compensating for the uncertainty in model inputs for a given period and addressing the most pressing satellite drag need—accurate specification and forecasts of density variability due to geomagnetic activity. Kalman Filter (Kalman, 1960) techniques have been developed to optimally combine the understanding captured in physical models with available data to specify and forecast the state of the system (Matsuo, et al., 2012 and references therein). Current thermospheric efforts necessarily involve assimilating limited high resolution satellite drag measurements into a first principles model to achieve more accurate global neutral density specification.

Supported by AFRL's Orbital Drag Environment program an assimilative model is being developed (Retterer, 2012) for an operational TIEGCM with a unique approach using an ensemble Kalman filter to ingest satellite drag and other data. The goal is to combine observational data and theoretical knowledge to obtain the more complete and accurate thermosphere-ionosphere description needed to meet Air Force requirements. The effort comprises several parts: the first-principles thermospheric and ionospheric models, the assimilation framework and the ingested data. Details will be provided in a separate report.

An initial test was done using the most recent version (1.9.4) of the TIEGCM model over 28 days starting on day 290, 2004 (and thus including the big storms of November 2004). Neutral densities were compared with CHAMP at the satellite location. The objective was examination of parameterizations of TIEGCM inputs for the assimilation process. The parameters first tried include 1) a scale factor for the solar EUV flux (sflxfac), 2) a scale factor between the solar-wind electric field and the Joule heating (joulefac), and 3) a factor for the eddy diffusivity (eddyfac). The choice of the first factor sflxfac is obvious. The second scale is chosen because the Joule heating is a nonlinear function of the electric field, which can be readily specified using higher temporal resolution (5 minute) solar-wind specification files from the ACE data. The third scale factor is selected because it is empirically specified, anyway. The idea is to adjust scale factors for various physical processes to capture the natural variability that isn't represented by the variation of the parameters used to drive the model. Trials were made with all possible combinations of 4 values of sflxfac, 3 values of joulefac, and three values of eddyfac. The parameter set producing the minimum error was selected as the optimal parameter choice for that day. This approach addresses how uncertain model parameters can be optimized to, on average, give the best agreement with observations. It will allow to best compare model variability including information about scale sizes with variability in observations to determine model fidelity. Finally it will improve observed

spatial/temporal model input parameters to get complete specification of the boundary conditions.

Initial tests using the parameters above found that this assimilation process could produce good agreement in the daytime or nighttime, but not in both portions of the local day simultaneously. If the daytime densities were right, then the nighttime densities would be too high. Some additional parameter was required. The relevant process must be one that reduces the density when there is no solar heating; given the uncertainties in rates, we adopted the NO cooling rate as an additional factor. To explore the effects of adjusting this rate, we employed the measured SEE solar spectrum to drive TIEGCM instead of using the EUVAC spectrum parameterized by F10.7, to eliminate one of the other adjustable factors.

Results for the accuracy of the TIEGCM model in reproducing CHAMP neutral density data when the density data were used to set simple scaling of parameters of the model are summarized in Figure 16 a-d. Figure 16a shows the density over several orbits during a portion of day 294, 2004, a geomagnetically quiet day for the CHAMP measurements and several unconstrained models. The top panel gives the mass density, the middle panel the satellite latitude, and the bottom panel the longitude (black curve) and local time (blue curve) of the satellite. In the top panel, the red curve is the mass density observed by CHAMP, the black curve is the model density from the empirical NRLMSIS model, the pink curve is TIEGCM using the measured SEE solar spectrum, while the blue and green curves are the TIEGCM using the EUVAC solar spectrum parameterized by F10.7. The model runs for green curve used the standard OMNI database for geophysical parameters (F10.7, Kp, ACE solar-wind parameters), while the model runs for the blue curve used a geophysical database at a finer time resolution. This figure shows that the parameterized solar spectrum EUVAC drives TIEGCM with noticeably poorer results than the measured solar spectrum. TIEGCM using SEE spectrum produces reasonable daytime densities but a reduced day/night dynamical range.

Figure 16b shows the same quantities as Figure 16a, but for the TIEGCM runs constrained by adjusting rate factors to better match the density data. The black and pink curves are again the MSIS and unconstrained TIEGCM/SEE runs. The blue curve is now the TIEGCM/SEE run with the NO cooling factor adjusted to improve the match with densities. This fitting required an increase in the NO cooling rate by about a factor of three; each day was adjusted individually, but the resulting NO cooling rate factor was about the same every day. For the run shown by the green curve, an additional factor, the Joule heating rate factor, was also permitted to vary. The improvement of the model fit was, however, minimal.

Figure 16c shows the statistical results over the whole 30-day trial for the TIEGCM model using a measured solar spectrum (the SEE data), so there was no degree of freedom for adjusting the solar radiation intensity. The blue points show the results when the scaling of the NO cooling rate was adjusted to give the best fit; the green points show the results fitting both the NO cooling rate and the scale factor of the Joule heating rate, while for comparison the pink points show the results for the TIEGCM densities when no

adjustment of any parameter was made, and the black points show the results for an empirical climatological model, MSIS. The top panel gives the daily mean density along the CHAMP orbit (red points), along with the TIEGCM model evaluated at those points. The second panel, labeled prediction efficiency, gives the difference between the mean-square variations of the density and the mean square error of the model calculation, normalized by the mean square variation of the density. Thus, if this quantity were unity, the model was able to track the variations of the measurements; smaller values are worse, and if the quantity is negative, then the errors in the model are worse than the natural fluctuations in the observed quantity. This plot shows that MSIS actually performs the best most of the time in predicting the variations of the density, but fails during the time of geomagnetic activity (days 312 – 316 of 2004). The fitted TIEGCM model performs adequately during the quiet days, but is the best during the period of geomagnetic activity. Fitting the Joule heating rate improves the performance only slightly (the green points are a little better than the blue ones); the 2-parameter fit may not be better because of the fine time step used, implying that the mean values describe the electric fields well. The final set of points (pink), are for the TIEGCM model without any adjustment, and they are the worst in accuracy. The other two panels of the plot show the mean and root-mean-square errors of the different model runs.

Finally, Figure 16d shows a sample of the difference in neutral winds at 240 km altitude between two model runs (fitted and unfitted) during an interval of geomagnetic activity. The constrained model had the NO cooling factor fitted to have its densities better match the CHAMP densities. Differences in winds over much of the globe have magnitudes up to 200 m/s. Because satellite drag depends on the velocity of the satellite relative to the ambient, these errors in winds contribute to the satellite errors we want to reduce.

## 7. Statistical Comparison of TIEGCM and Empirical Models

A statistical analysis of data vs TIEGCM version 1.91 provides a more quantitative estimate of the model capability to describe thermosphere variability. We use CHAMP 2002-2005 and SETA-2 1982 point density values and focus on the northern hemisphere since that is where SETA is most accurate. Data are first sorted into day and night local time bins; 6-18 hours day and not within 6-18 hours for night for CHAMP. SETA day and night bins are approximately 1030 and 2230 respectively. Following the day /night binning, all data are sorted into six ap bins: 0-10, 10-25, 25-50, 50-100, 100-200 and 200-400. We then examine the low ap bin and the two highest ap bins combined (ap>100) as a function of latitude. In this part of the study the data are put into 10 degree geographic latitude bins. Then a mean and standard deviation are calculated for each bin. We then compared CHAMP and SETA data to TIEGCM, JB08 and other models that were described in other studies (Marcos, et al., 2009). CHAMP data come from an AFRL report to Rand Corp (Marcos, et al., 2009); SETA data are from Marcos and Forbes, 1985. This provides a measure of how well the physical model used in this TM compares to the current operational model. Assimilation results were not used in this comparison. The comparison may generally not match exactly for the databases, but differences should be small.

Figure 17a shows CHAMP to TIEGCM mean ratios (top) and standard deviations (bottom) for day (left) and night (right) local time bins. Day data are in blue and night data are in red. Note that the data for each ap bin are plotted at the beginning interval of the bin, rather than in the middle. The mean values increase with increased ap, from about 1 in the lowest bin to about 1.3 in the highest bins, indicating the observed underestimation of the density response with increasing geomagnetic activity. Similarly, the standard deviations increase with geomagnetic activity as would be expected from about 25% for the 0-10 ap bin to about 31% for ap > 100. Dayside means tend to be about 10% higher than night means apparently reflecting the higher nighttime model densities implied in semiannual variation, solar cycle and assimilation studies described previously. Standard deviations tend to be about 4% lower during daytime. In Figure 17b, for comparison, CHAMP mean ratios to JB08 are similar; being about 1.07 in the 0-10 ap bin and very close to unity above ap of 100. Standard deviations increase from 16% to 27% over the ap range (Marcos, et al., 2009). Figure 17b shows CHAMP vs empirical models (Marcos, et al., 2009) for the same time period, but with no hemisphere or local time binning. The JB08 model is in green; NRLMSIS and JB06 are purple and orange respectively. JB08 and NRLMSIS means are close to unity for all bins, but JB06 shows a decrease of about 20%. Standard deviations for JB08 increase from about 16% (lowest ap bin) to about 27% (highest ap bin) and are therefore about 9% lower for the lowest bin and only four percent lower for high geomagnetic activity. Both JB08 and NRLMSIS have standard deviations of about 32% in the highest bin. It is noted again that each ap bin in this figure contains data for all latitudes and local times; finer binning could reduce errors.

Figure 18a shows CHAMP data in 10 degree latitude bins (data for each bin plotted at start of interval) for day, left side and night, right side. Mean values are at the top and standard deviations are at the bottom. For each chart data are plotted for the lowest ap bin (blue) and ap>100 (red). Means are fairly constant vs latitude on the dayside and increase by about 15% for high ap on the nightside. Nightside errors are higher than those on the dayside for both ap bins. Day errors increase from about 24% to 36% whereas the night values increase from about 29% to 37%. Figure 18b shows CHAMP vs JB08 means (top) and standard deviations (bottom). Mean values tend to increase by about 10% from low to high ap. Standard deviations increase from about 15% to 19% at low ap with increasing latitude. For high ap, errors increase from about 25% to 37% for ap 100-200 but drop to 19% for the highest bin, possibly reflecting impact of the new geomagnetic storm algorithm implemented in JB08 (Burke, et al., 2007). Note that at high southern hemispheres the error is ~26%. Thus TIEGCM errors in the 100-200 ap bin are similar to those for JB08 the northern hemisphere. For the ap >200 case, JB08 errors are lower.

SETA-2 to TIEGCM data in Figure 19a also show mean ratios at top and standard deviation at bottom. Blue points are daytime data and red are for nighttime bins. Mean ratios in the northern hemisphere increase on average from about 0.96 to 1.2 as ap increases from lowest to highest ap bin and standard deviations rise from 11 to 18%. These lower standard deviations are assumed to be mainly an altitude effect, consistent with one-day average drag data showing that the standard deviation increases with altitude from about 10% at 220 km to ~15% at 400 km (Marcos, et al., 2006). Local time

variations are small; daytime errors are a few percent higher in the two highest ap bins. Corresponding JB08 (green data) means for day local times in the northern hemisphere in Figure 19 were fairly constant varying from about 0.94 to 1.02 over the ap span (Lin, et al., 2011). Standard deviations varied from 16 to 21% from lowest to highest bin values. Increases in error with increases in ap bin for JB08 (green points) are very similar to those of J70 (red squares). There is not an improvement for JB08 in the higher ap bins as was observed for CHAMP.

Figure 20a shows SETA-2 data in 10 degree latitude bins (data for each bin plotted at start of interval) for day, left side, and night, right side. Mean values are at the top and standard deviations are at the bottom. For each chart data are plotted for the lowest ap bin (blue) and  $ap > 100$  (red). The night values are higher than those for day in all cases. The difference may be due to modeling or to a bias in the SETA processing. Reference to Figure 5 shows an average dayside altitude of  $\sim 185$  km and an average nightside altitude  $\sim 230$  km. In the high ap bin, standard deviations from equator to pole increase for TIEGCM ratios from 14 to 28% (day) and 19 to 26% (night). Ratios to JB08 are in Figure 20b for three models. The JB08 errors for the highest ap bin (left figures) increase from 11% to 20%. Thus the JB08 model errors vs latitude are smaller overall.

## 8. Summary

General Circulation Models have been a critical research tool for interpreting data and advancing understanding physics of the thermosphere and ionosphere. Simulations depend on the model inputs and boundary conditions, including, as noted in Section 1c, solar radiation, magnetospheric currents, auroral particle fluxes, and global-scale atmospheric waves from below. There are large uncertainties in these highly variable inputs at any given time. Observations are relatively sparse, and temporal/spatial extrapolation of the observations to adequately specify boundary conditions is difficult. Validation efforts determine fidelity of models and guide further development. This preliminary assessment of TIEGCM version 1.9.1 using global neutral density measurements from satellite accelerometer data has shown:

- a. Solar cycle variations: TIEGCM overestimates density during periods near solar activity minimum, as do empirical models since in both cases the solar input was parameterized by the F10 index. The model has the capability to input high resolution solar EUV data. Implementation of selected lines has shown promise to improve specification but the wavelengths and their relative importance need further study. Detailed forthcoming solar irradiance measurements from the EVE experiment on SDO will eventually permit the full capability of physical models to represent thermosphere response to variations in solar EUV. We note that EUV bursts from solar flares, not described in this Memo, are another source of abrupt density perturbations (Sutton, et al., 2006). Qian and Solomon, 2012 have shown that TIEGM has the capability to handle these given the correct inputs.
- b. Semiannual variations: The physics for this effect did not fall out of V 1.9.1 and earlier versions of this model. An empirical seasonally dependent eddy diffusion coefficient at

90 km deduced from satellite drag data near 400 km was invoked to give a realistic TIEGCM response in version 1.9.4. A theoretical solution using gravity waves and tides is being sought. The trend of long term semiannual variations can be modeled in an operational forecast scheme. If irregular contributions that perturb this trend can be accounted for, then physical models would exceed the capability of empirical models for density semiannual forecasts.

c. Local time variations: Nightside (18-06 hrs) TIEGCM model to data ratios are on average ~15% higher than on the dayside. Data assimilation suggested that the physical model cooling rates need adjustment. The feature was also found in TIEGCM model V 1.9.4. This effect requires further study.

d. Geomagnetic storms: TIEGCM simulations tended to underestimate storm response at low and high thermospheric altitudes due to lack of accuracy of heating drivers, mainly the quality of input electric fields. On-going data assimilation efforts show that can geomagnetic storm density errors (as well as those due to other effects) significantly reduce these errors.

e. The current statistical accuracy of TIEGCM is approaching that of empirical models from CHAMP altitudes down to the reentry region. This very encouraging finding is consistent with validation efforts of other physical models at CHAMP altitudes outside the scope of this memo (e.g. Codrescu, et al., 2012; Shim, et al., 2011).

The ultimate goal of satellite drag research is to implement an accurate assimilative, operational, physics based forecast model with 5% accuracy and 3-5 day forecasts. With much new understanding of the atmosphere being developed, physics-based modeling tools currently are the future tool for density specification and prediction. Physics-based models offer an advantage by providing more detailed, time-dependent structure not available in the semi-empirical models. The use of input proxies for solar UV and EUV radiation, of statistical patterns of particle precipitation and plasma convection for the calculation of Joule heating, and of seasonal averages for the amplitude and phase of waves propagating from below leads to large uncertainties in model predictions. Extensive research on the required fundamental heating processes resulting from the EUV and solar wind interaction with the coupled magnetosphere-ionosphere-thermosphere system continues. Geomagnetic storms remain the biggest challenge. Much of our imperfect understanding is due to lack of observational data on high latitude heating mechanisms. Joule heating is the dominant heating mechanism affecting the neutral density during disturbed conditions. Knowing its magnitude and spatial distribution is important for the accuracy of neutral density specification and atmospheric drag determination.

The challenges facing operational physical models are scientific, requiring new space environment theories of solar phenomena, their propagation through the interplanetary environment and their interaction with the Earth's thermosphere-ionosphere-magnetosphere system and new space environment measurements. The problems for space weather predictions are analogous to those addressed by tropospheric weather for

which the basic physics has been known for decades. In spite of knowing how the equations work, they require input, hence the need for operational weather satellites. Observations are critical to unravel the basic physical mechanisms to build better models with improved predictions, but there will always be a need for input to the models. The alternative to measuring the inputs on the necessary temporal and spatial scales is to leverage all available measurements of state parameters and steer the model results in the right direction using a data assimilation scheme.

Results from the AFOSR MURI NADIR effort headed by the University of Colorado (see University of Colorado MURI website for complete description) are an obvious resource to be assimilated into operational physical modeling. The MURI team has developed research products that can be transitioned into operational models. Some transition highlights were reviewed by Fuller-Rowell and Forbes, 2010. The fundamental next step after the MURI is to incorporate the benefits of a physical model within the assimilation process. In the future, solar wind and magnetosphere models may be able to predict important external drivers for thermosphere-ionosphere models, so a few hours to a few days forecast of the Joule heating index and therefore neutral density would be feasible. The MURI program attempts to address these model limitations through scientific analyses of solar phenomena and available satellite drag data. Initiating the physical model with both direct in-situ and indirect observations in a statistically rigorous manner provides a practical approach for representing the time-dependent conditions of the thermosphere. Implementation of a Kalman filtering data assimilation technique by the space physics community has proven to be non-trivial. It requires detailed understanding of the physics based model as well as estimation theory and astrodynamics. Thus, this development requires cooperative efforts of the space physics and astrodynamics communities. AFRL has demonstrated application of the technique reduces errors during a major geomagnetic storm.

In summary, uncertainties in neutral density variations have been the major error source for LEO determination. The problem is being vigorously and fruitfully attacked by numerous space weather studies including physical modeling research, data assimilation schemes, predictive solar and geomagnetic indices, upward propagating waves and in-situ measurements. While there is still a lot of research needed, the tools are finally becoming available. The culmination of these efforts will be steady progress in meeting the evolving, previously unattainable, stringent requirements for operations in the satellite drag environment.

## References

- Akmaev, R. A. (2011), Whole atmosphere modeling: Connecting terrestrial and space weather, *Rev. Geophys.*, 49, RG4004, doi:10.1029/2011RG000364.
- Akmaev, R. A., T. J. Fuller-Rowell, F. Wu, J. M. Forbes, X. Zhang, A. F. Anghel, M. D. Iredell, S. Moorthi, and H.-M. Juang (2008), Tidal variability in the lower thermosphere: Comparison of Whole Atmosphere Model (WAM) simulations with observations from TIMED, *Geophys. Res. Lett.*, 35, L03810, doi:10.1029/2007GL032584.
- Anderson, Rodney L., George H. Born, and Jeffrey M. Forbes (2009), Sensitivity of orbit predictions to density variability, *J. Spacecraft and Rockets*, 46, pp. 1214-1230, doi:10.2514/1.41238.
- Bowman, B. R., W. K. Tobiska, F. A. Marcos, and C. Valladares (2008), The JB2006 empirical thermospheric density model, *J. Atm. and Solar-Terr Phys.*, 70, pp. 774-793.
- Bowman, B. R., W. K. Tobiska, F. A. Marcos, C. Y. Huang, C. S. Lin, and W. J. Burke (Aug. 2008), A new empirical thermospheric density model JB2008 using new solar and geomagnetic indices, AIAA 2008-6438, AIAA/AAS Astrodynamics Specialist Conference, Honolulu, HI.
- Burke, W. J., C. Y. Huang, F. A. Marcos, and J. O. Wise (2007), Interplanetary control of thermospheric densities during large magnetic storms, *J. Atmos. Solar-Terr. Phys.*, 69, p. 279.
- Burns, A.G., T.L. Killeen, W. Wang, and R.G. Roble (2004), The solar-cycle-dependent response of the thermosphere to geomagnetic storms, *J. Atm. Solar-Terr. Phys.*, 66, pp. 1-14.
- Codrescu, M. V., C. Negrea, M. Fedrizzi, T. J. Fuller-Rowell, A. Dobin, N. Jakowsky, H. Khalsa, T. Matsuo, and N. Maruyama (2012), A real-time run of the Coupled Thermosphere Ionosphere Plasmasphere Electrodynamics (CTIPE) model, *Space Weather*, 10, S02001, doi:10.1029/2011SW000736.
- Deng, Y., Y. Huang, S. Solomon, L. Qian, D. Knipp, D. R. Weimer, and J.-S. Wang (2012), Anomalously low geomagnetic energy inputs during 2008 solar minimum, *J. Geophys. Res.*, 117, A09307, doi:10.1029/2012JA018039.
- Dickinson, R. E., E. C. Ridley, and R. G. Roble (1981), A three-dimensional general circulation model of the thermosphere, *J. Geophys. Res.*, 86, pp. 1499-1512.
- Dickinson, R. E., E. C. Ridley, and R. G. Roble (1984), Thermospheric general circulation with coupled dynamics and composition, *J. Atmos. Sci.*, 41, pp. 205-219.



Emmert, J. T., J. M. Picone, J. L. Lean, and S. H. Knowles (2004), Global change in the thermosphere: Compelling evidence of a secular decrease in density. *J. Geophys. Res.*, 109, DOI: 10.1029/2003JA010176.

Emmert, J. T., J. L. Lean, and J. M. Picone (2010), Record-low thermospheric density during the 2008 solar minimum, *Geophys. Res. Lett.*, 37, L12102, doi:10.1029/2010GL043671.

Forbes, J.M. (2007), Dynamics of the thermosphere, *J. Meteorol. Soc. Japan*, 85B, pp. 193-213.

Forbes, J. M., S. L. Bruinsma, X. Zhang, and J. Oberheide (2009), Surface-exosphere coupling due to thermal tides, *Geophys. Res. Lett.*, 36, L15812, doi:10.1029/2009GL038748.

Fuller-Rowell, T. J., M. Codrescu, and S. Queagan (1996), On the seasonal response of the thermosphere and ionosphere to geomagnetic storms, *J. Geophys. Res.*, 101(A2), pp. 2343-2353.

Fuller-Rowell, T. J. and Jeff Forbes (2010), NADIR: Neutral Atmosphere Density Interdisciplinary Research - Recent progress and transition Plans, Space Weather Week, Boulder, CO.

Guo, J., W. Wan, J. M. Forbes, E. Sutton, R. S. Nerem, and S. Bruinsma (2008), Interannual and latitudinal variability of the thermosphere density annual harmonics, *J. Geophys. Res.*, 113, A08301, doi:10.1029/2008JA013056.

Hedin, A. E. and H. G. Mayr (1987), Characteristics of wavelike fluctuations in Dynamics Explorer neutral composition data, *J. Geophys. Res.*, 92(A10), pp. 11,159-11,172, doi:10.1029/JA092iA10p11159.

Jacchia, L.G (1964), Static diffusion models of the upper atmosphere with empirical temperature profiles, SAO Special Report No. 170.

Jacchia, L. G. (1970), Revised static models of the thermosphere and exosphere with empirical temperature profiles, SAO Special Report No. 313.

Kalman, R. E. (1960), A new approach to linear filtering and prediction problems, *J. Basic Eng.*, 82, pp. 34-45.

Knipp, D. J., Devin Della-Rose, Omar Nava, and W. Kent Tobiska (2005), Long- and short-term variations in thermospheric heating sources, AAS 05-253, AIAA Astrodynamic Specialists Conference, Lake Tahoe, CA.

Lean, J. L. (1997), The Sun's variable radiation and its relevance for Earth, *Ann. Rev. Astron. Astrophys.*, 35, pp. 33-67, doi:10.1146/annurev.astro.35.1.33.

- Lei, J., T. Matsuo, X. Dou, E. Sutton, and X. Luan (2012), Annual and semiannual variations of thermospheric density: EOF analysis of CHAMP and GRACE data, *J. Geophys. Res.*, 117, A01310, doi:10.1029/2011JA017324.
- Lin, C. S., Loren C. Chang, and Samuel B. Cable (27 April 2010), Validation of physics-based neutral density modeling using TIEGCM, Space Weather Workshop, Boulder, CO.
- Marcos, F.A. and J.M. Forbes (1985), Thermospheric winds from the satellite electrostatic triaxial accelerometer system, *J. Geophys. Res.*, v. 90, p. 6543.
- Marcos, F.A., M. Kendra, J. Griffin, J. Bass, J. Liu, and D. Larson (1998), Precision low earth orbit determination using atmospheric density calibration, *Jnl Astronautical Sciences*, 46, p. 395.
- Marcos, F. A., B. R. Bowman, and R.E. Sheehan (2006), Statistical evaluation of the Jacchia-Bowman 2006 thermospheric neutral density model, AIAA 2006-6166, AIAA Astroynamics Conference, Keystone, CO.
- Marcos, Frank A., Cheryl Y. Huang, Chin S. Lin, John M. Retterer, and Susan H. Delay (2009), Evaluation of recent thermospheric neutral density models, Unpublished Manuscript.
- Matsuo, T., M. Fedrizzi, T. J. Fuller-Rowell, and M. V. Codrescu (2012), Data assimilation of thermospheric mass density, *Space Weather*, 10, S05002, doi:10.1029/2012SW000773.
- Paetzold, H. K. and H. Zschörner (1961), An annual and a semiannual variation of the upper air density, *Pure Appl. Geophys.*, 48, pp. 85-92, doi:10.1007/BF01992371.
- Qian, L., S.C. Solomon, R.G. Roble, B.R. Bowman, and F.A. Marcos (2008), Thermospheric neutral density response to solar forcing, *Adv. Sp. Res.* 42, pp. 926-932.
- Qian, Liying, Stanley C. Solomon, and Timothy J. Kane (2009), Seasonal variation of thermospheric density and composition, *J. Geophys. Res.*, 114, A01312, doi:10.1029/2008JA013643.
- Qian, Liying and Stanley C. Solomon (2012), Thermospheric Density: An overview of temporal and spatial variations, *Space Science Reviews*, Volume 168, Issue 1-4, pp. 147-173.
- Rhoden, E. A., J. M. Forbes, and F. A. Marcos (2000), The influence of geomagnetic and solar variabilities on lower thermosphere density", *J. Atm. Solar-Terr. Phys.*, 62, pp. 999-1013.

- Richmond, A. D., E. C. Ridley, and R. G. Roble (1992), A Thermosphere/Ionosphere General Circulation Model with coupled electrodynamics, *Geophys. Res. Lett.*, 19, pp. 601-604.
- Roble, R.G. (1977), "The Thermosphere", *The Upper Atmosphere and Magnetosphere*, National Academy of Sciences, Washington, D.C.
- Roble, R. G. and E. C. Ridley (1987), An auroral model for the NCAR thermospheric general circulation model (TGCM), *Annales Geophys.*, 5A, pp. 369-382.
- Roble, R. G., E. C. Ridley, and R. E. Dickinson (1987), On the global mean structure of the thermosphere, *J. Geophys. Res.*, 92, pp. 8745-8758.
- Roble, R. G., E. C. Ridley, A. D. Richmond, and R. E. Dickinson (1988), A coupled thermosphere/ionosphere general circulation model, *Geophys. Res. Lett.*, 15, pp. 1325-1328.
- Roble, R. G. and E. C. Ridley (1994), A thermosphere-ionosphere-mesosphere-electrodynamics general circulation model (TIME-GCM): equinox solar cycle minimum simulations (30-500 km), *Geophys. Res. Lett.*, 21, pp. 417-420.
- Sentman, L. H. (1961), Free molecule flow theory and its application to the determination of aerodynamic Forces, Lockheed Missile and Space Co., LMSC-448514, AD 265-409 (available from National Technical Information Service, Springfield, VA).
- Shim, J., M. Kuznetsova, L. RastaJer, and M. Hesse (2011), Systematic assessment of ionosphere/thermosphere models using metrics, AGU Chapman Conference on Modeling the Ionosphere/Thermosphere System, Charleston, South Carolina, USA .
- Solomon, Stanley C., Alan Burns, Barbara Emery, Ben Foster, Astrid Maute, Liying Qian, and Art Richmond (2012), TIE-GCM Updates, The NCAR Thermosphere-Ionosphere-Electrodynamics General Circulation Model at the Community Coordinated Modeling Center, CCMC Workshop.
- Solomon, Stanley C., Thomas N. Woods, Leonid V. Didkovsky, John T. Emmert, and Liying Qian (2010), Anomalous low solar extreme-ultraviolet irradiance and thermospheric density during solar minimum, *Geophys. Res. Lett.* 37, L16103, doi:10.1029/2010GL044468.
- Storz, M. F., B. R. Bowman, and Maj. J. I. Branson (2002), High Accuracy satellite Drag Model (HASDM) AIAA 2002-4886, AIAA/AAS Astrodynamics Specialist Conference, Monterey, CA.
- Sutton, E. K., R. S. Nerem, and J. M. Forbes (2007), Atmospheric density and wind measurements deduced from accelerometer data, *J. Spacecraft and Rockets*, 44(6), doi:10.2514/1.28641.

Sutton, E. K. (2009), Normalized Force Coefficients for Satellites with Elongated Shapes, *J. Spacecraft and Rockets*, 46(1), pp. 112-116, doi:10.2514/1.40940.

Sutton, E. K., J. M. Forbes, R. S. Nerem, and T. N. Woods (2006), Neutral density response to the solar flares of October and November, 2003, *Geophys. Res. Lett.*, 33, L22101, doi:10.1029/2006GL027737.

Tapley, B. D., S. Bettadpur, M. Watkins, and C. Reigber (2004), The Gravity Recovery and Climate Experiment: Mission overview and early results, *Geophys. Res. Lett.*, 31(9), L09607, doi:10.1029/2004GL019929.

Weimer, D. R. (2005), Improved ionospheric electrodynamic models and application to calculating Joule heating rates, *J. Geophys. Res.*, 110, A05306, doi:10.1029/2004JA010884.

Woods, T. N., F. G. Eparvier, R. Hock, A. R. Jones, D. Woodraska, D. Judge, L. Didkovsky, J. Lean, J. Mariska, H. Warren, D. McMullin, P. Chamberlin, G. Berthiaume, S. Bailey, T. Fuller-Rowell, J. Sojka, W. K. Tobiska, and R. Viereck (2012), Extreme Ultraviolet Variability Experiment (EVE) on the Solar Dynamics Observatory (SDO): Overview of science objectives, instrument design, data products, and model developments, *Solar Physics*, Volume 275, Issue 1-2, pp. 115-143.

## Appendix: Figures

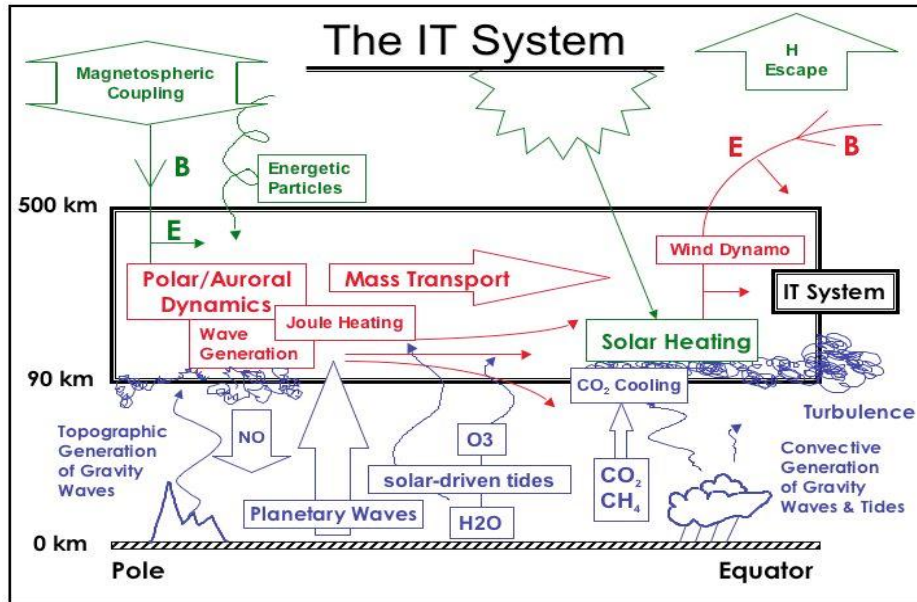


**Figure 1: Thermosphere Heating and Dynamics Processes.**

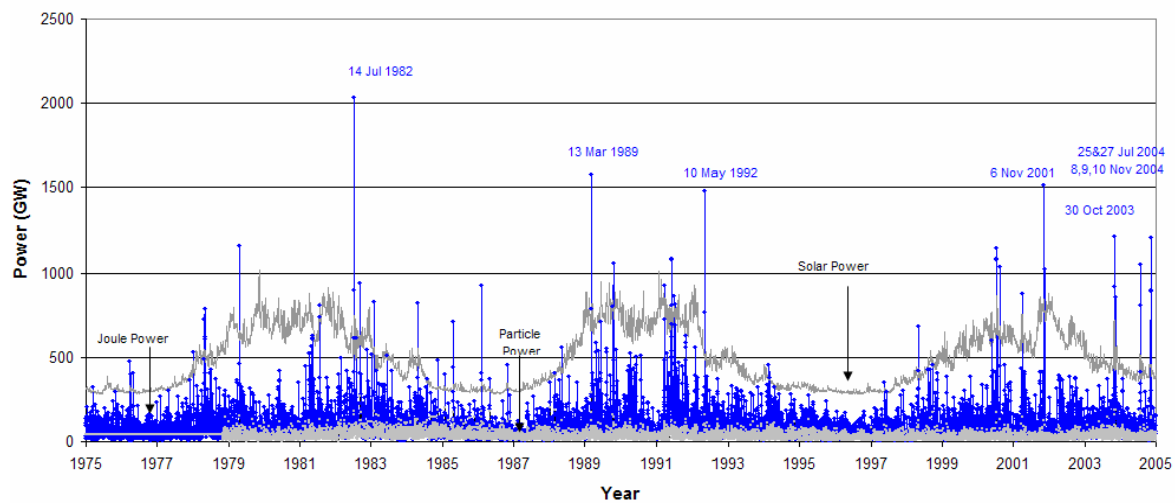


**Figure 2: Solar electromagnetic and solar wind heating into thermosphere.**

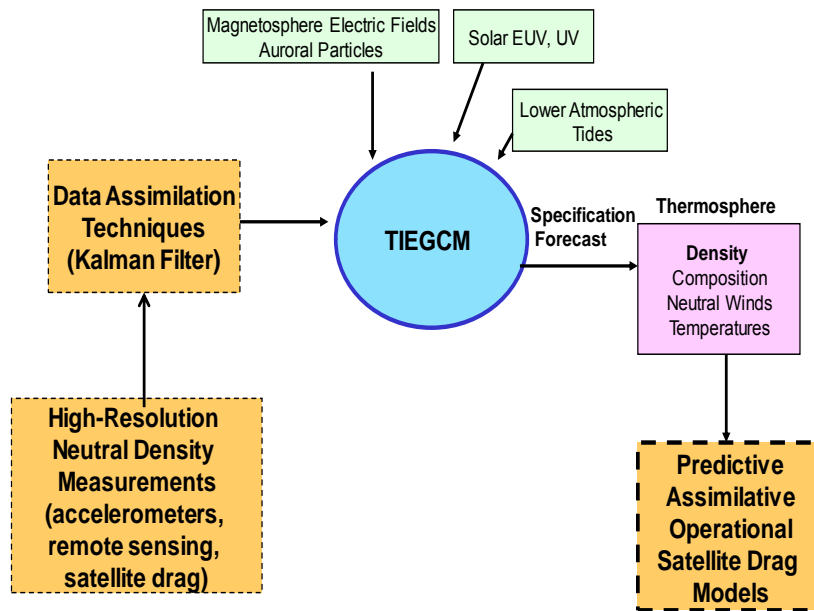


**Figure 3: Assimilative Physics-Based Neutral Density Models.**

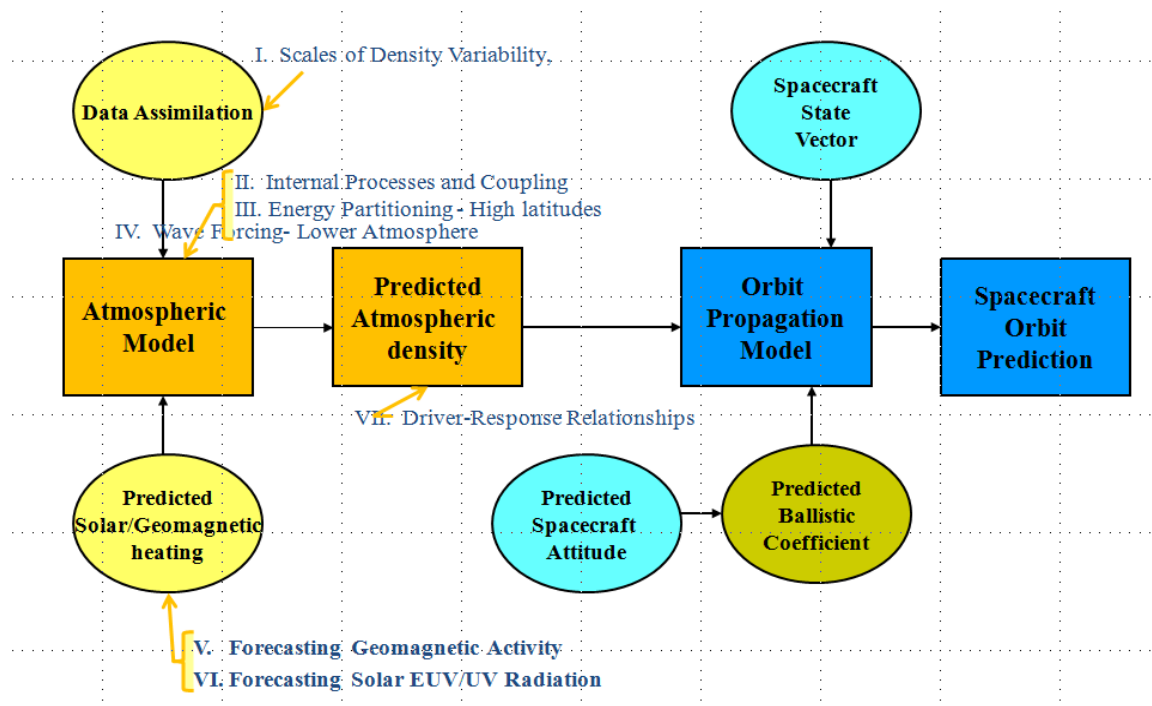


**Figure 4: Solar activity and spacecraft orbital prediction.**

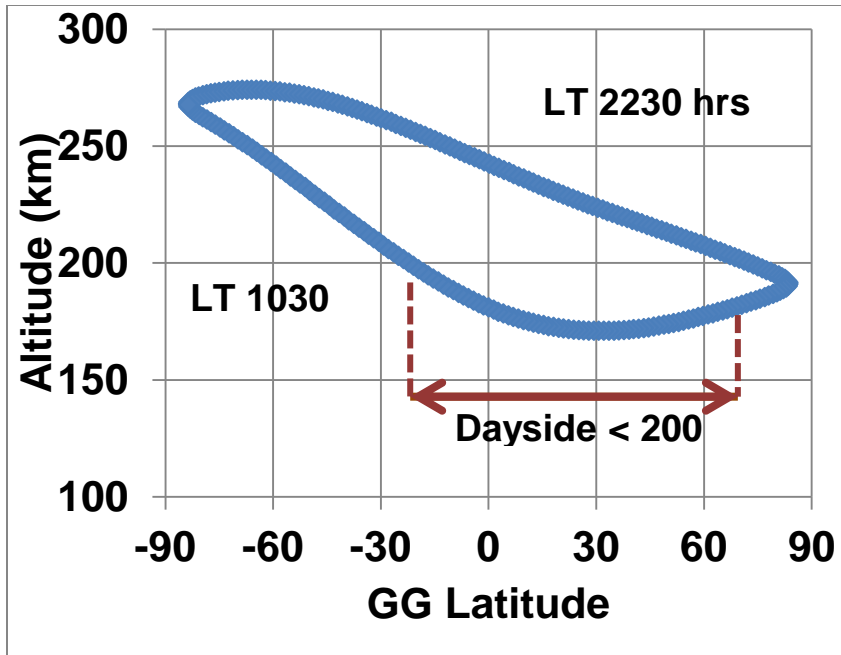


Figure 5: Typical orbital parameters for the SETA missions.

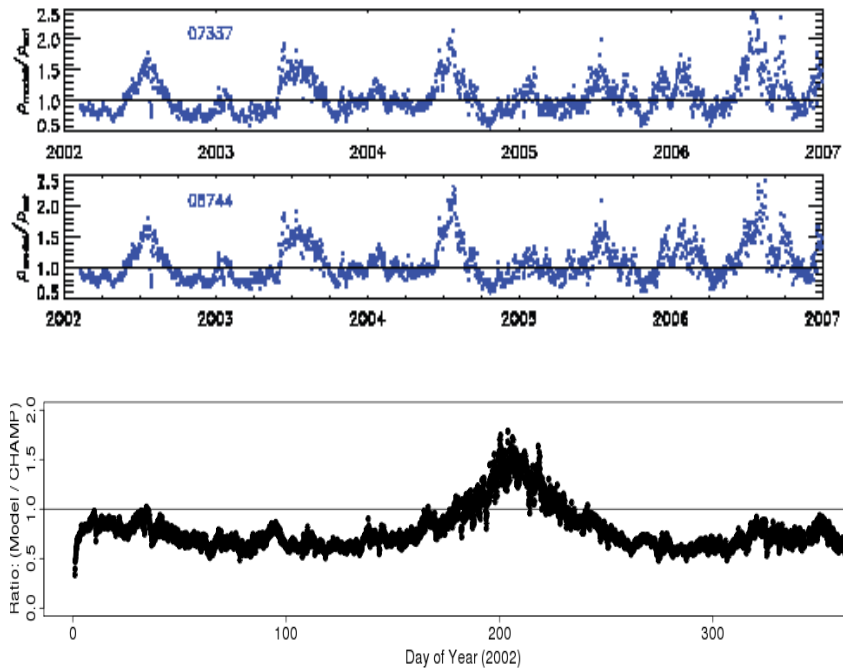
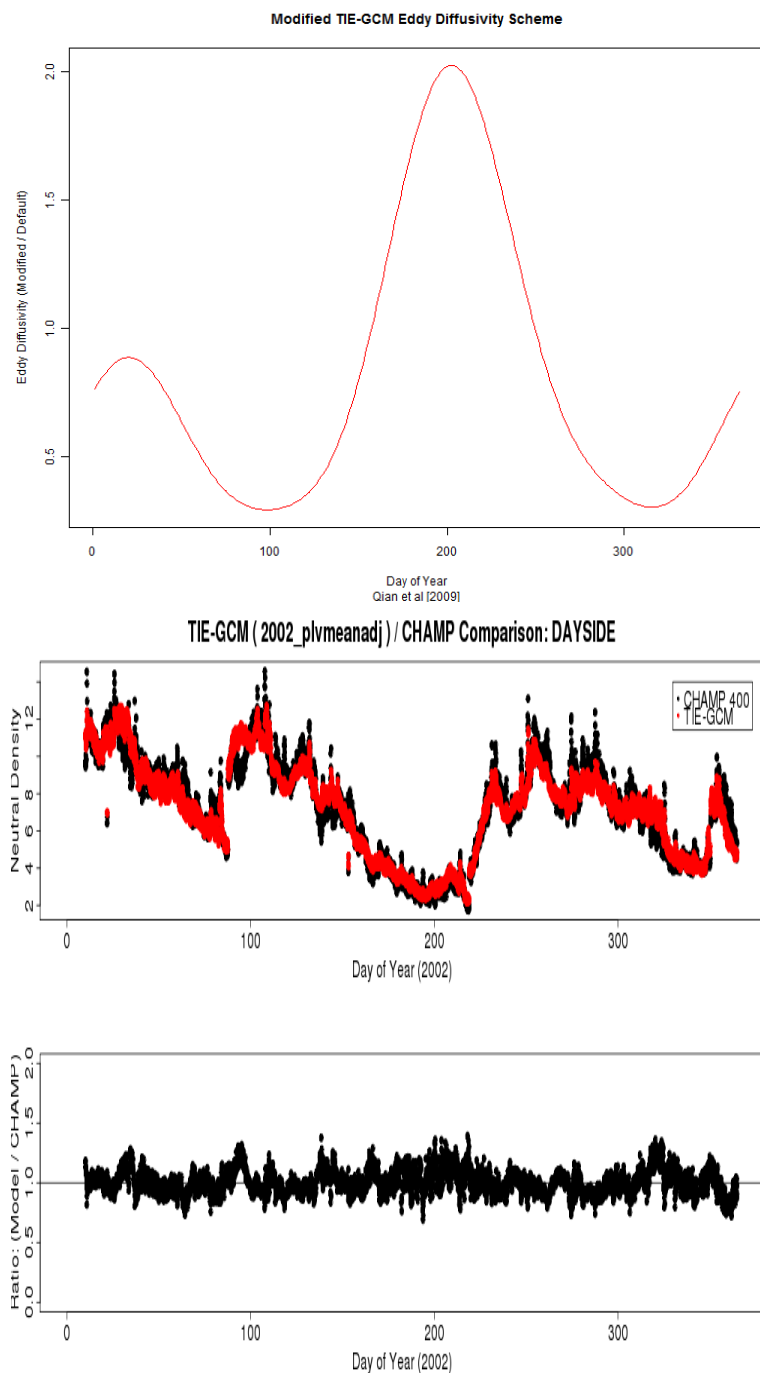


Figure 6: TIGCM underestimation of density at solstices for (top) satellite drag measured by two different satellites showing model/data ratio vs time and (Bottom) model to density from CHAMP accelerometer in 2002.



**Figure 7: Top: Variable eddy diffusion coefficient imposed on TIEGCM. Middle: Revised model densities vs CHAMP density data. Bottom: Revised model/CHAMP ratios.**



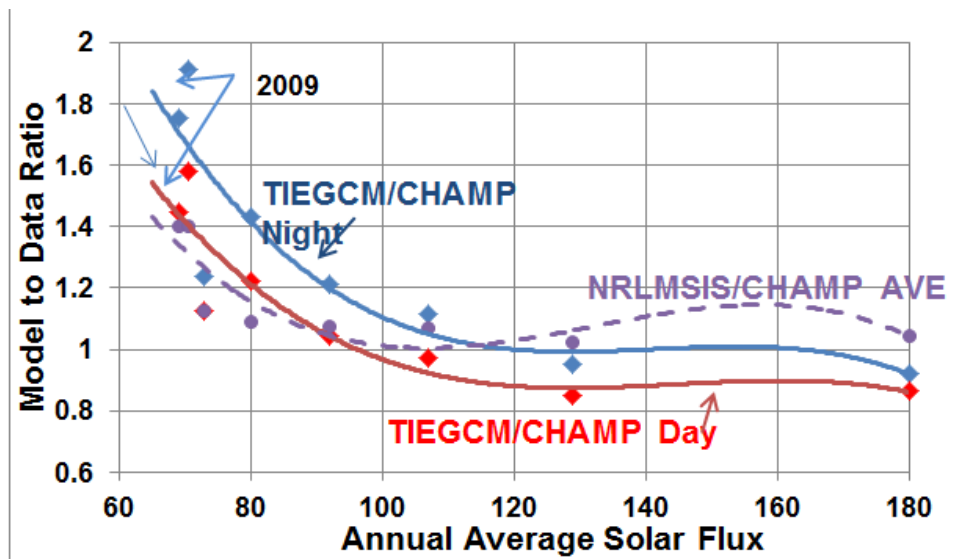


Figure 8a: Solar cycle variation of TIEGCM and NRLMSIS annual mean values.

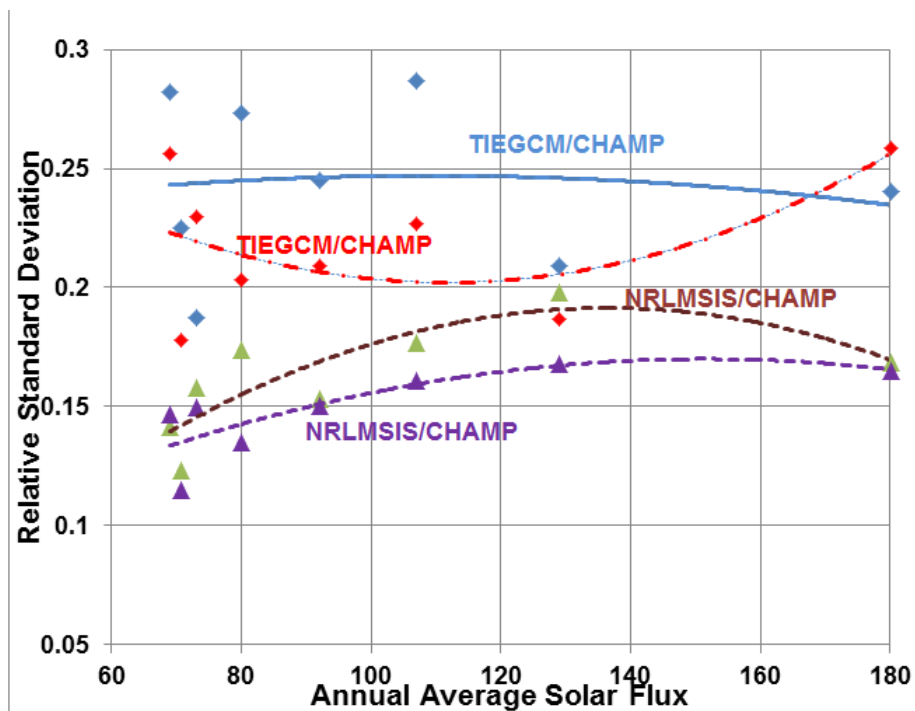
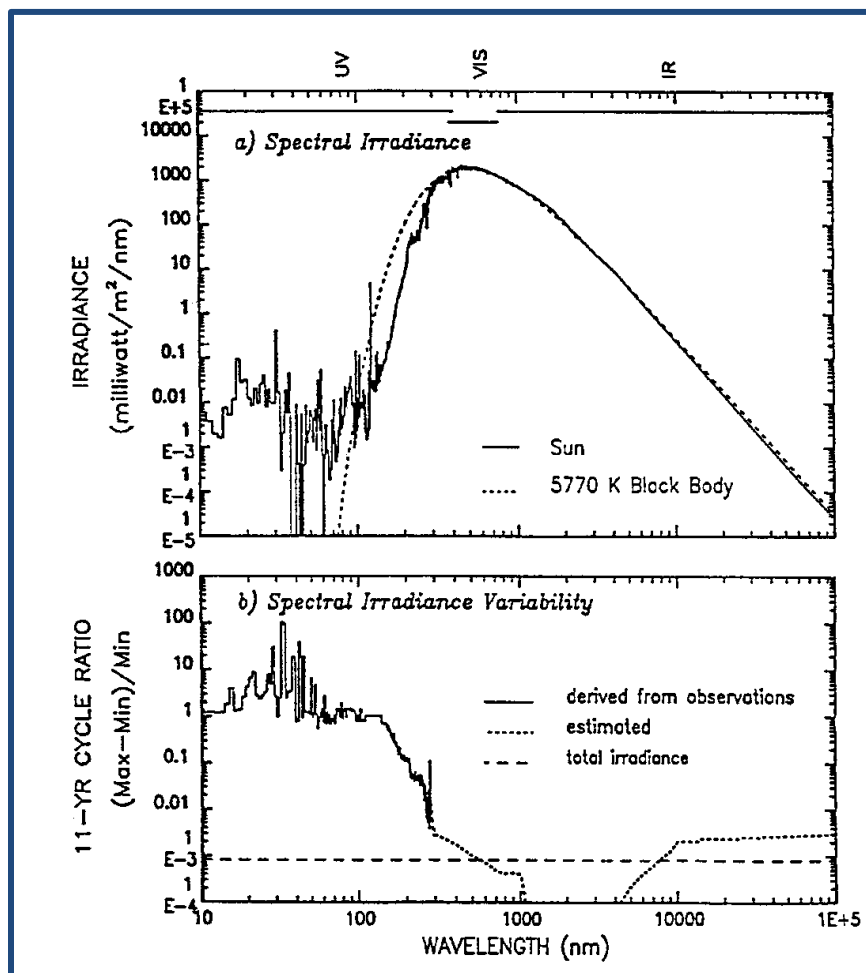
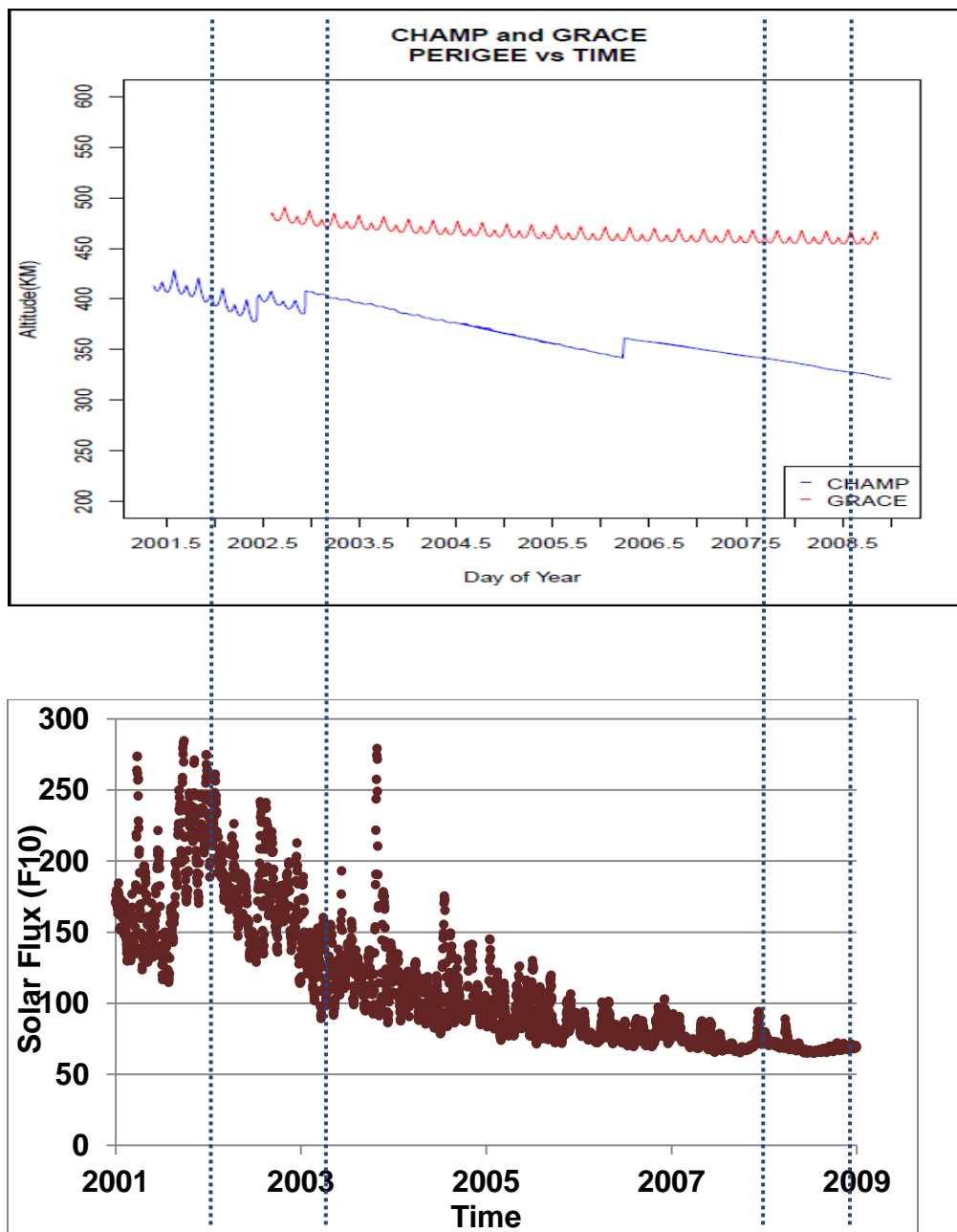


Figure 8b: Solar cycle variation of TIEGCM and NRLMSIS standard deviations.



**Figure 8c: Top: Solar spectral radiance; Bottom: Ratio of solar maximum to solar minimum radiance vs wavelength.**



**Figure 9: CHAMP & GRACE perigee altitude (top) and solar flux (bottom) vs time. Blue dashed lines indicate periods studied.**

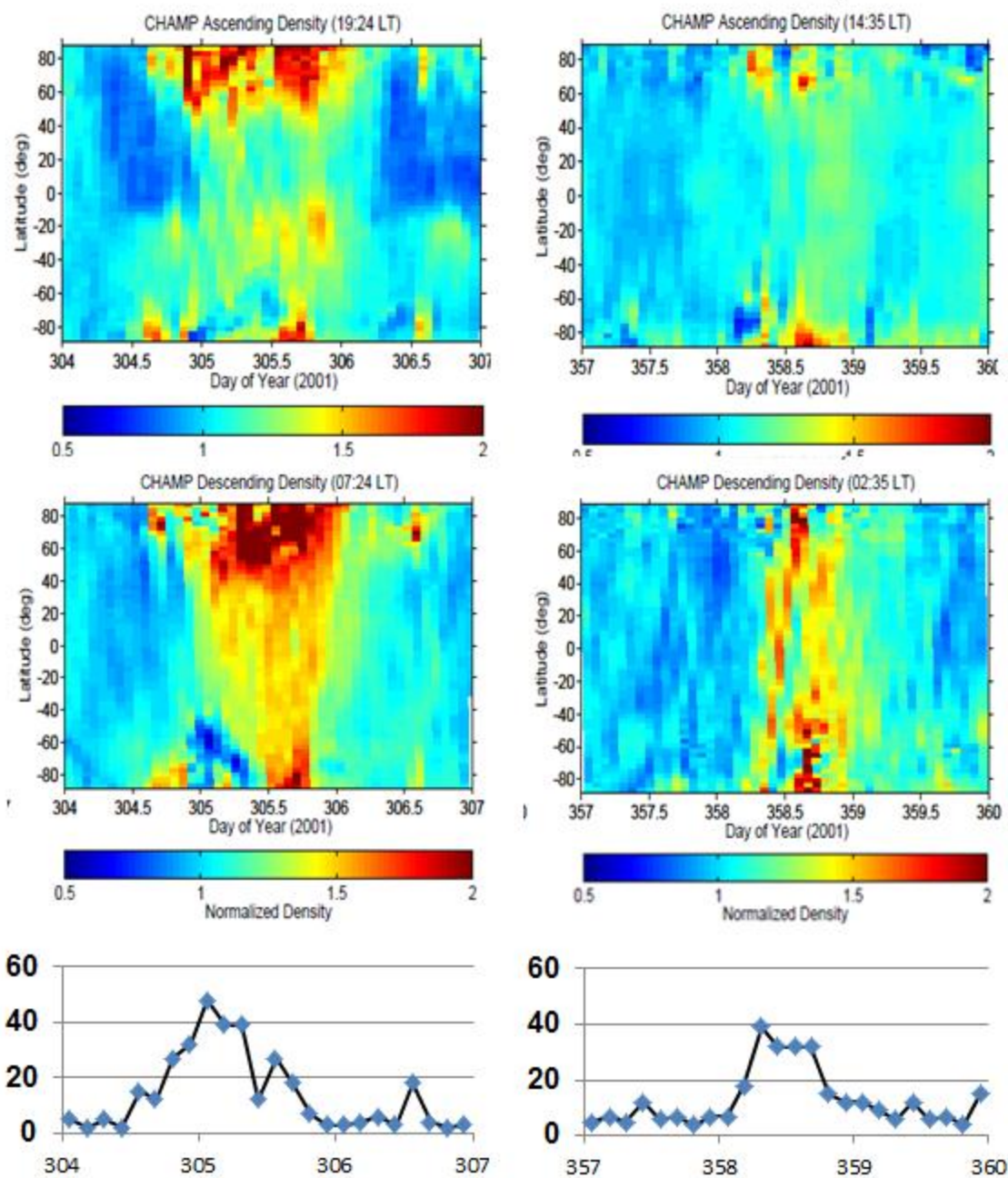


**Figure 10a: CHAMP 2001 geomagnetic storm responses at high solar flux. Left top and middle panels are for period starting day 304; right top and middle panels are for periods starting day 357. Bottom panels are respective  $a_p$  values.**

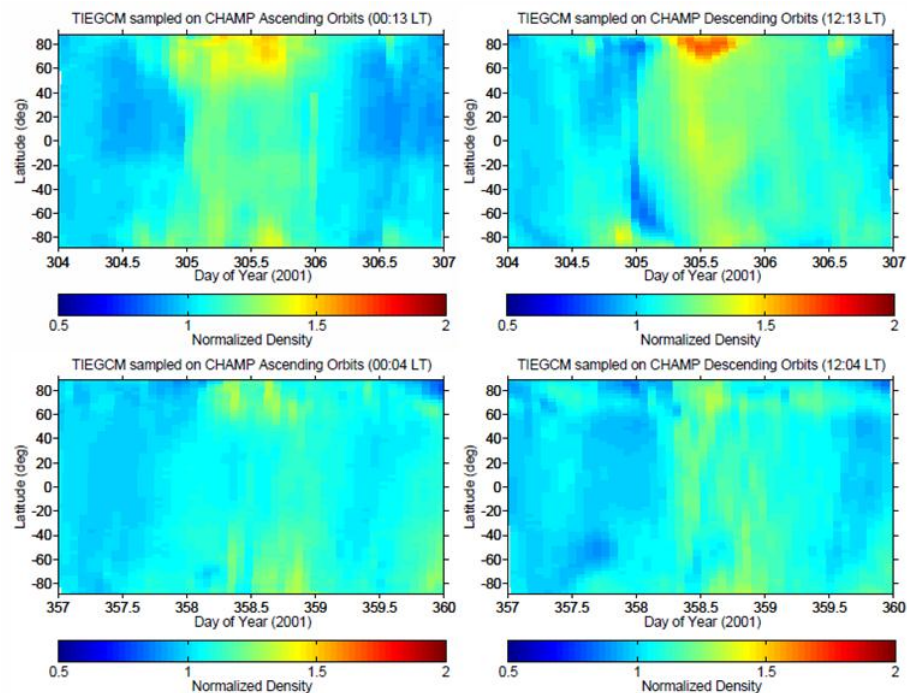


**Figure 10b: TIEGCM simulations of two storms in Figure 10a. Storm 1 is in top two panels; storm 2 is in bottom two panels.**

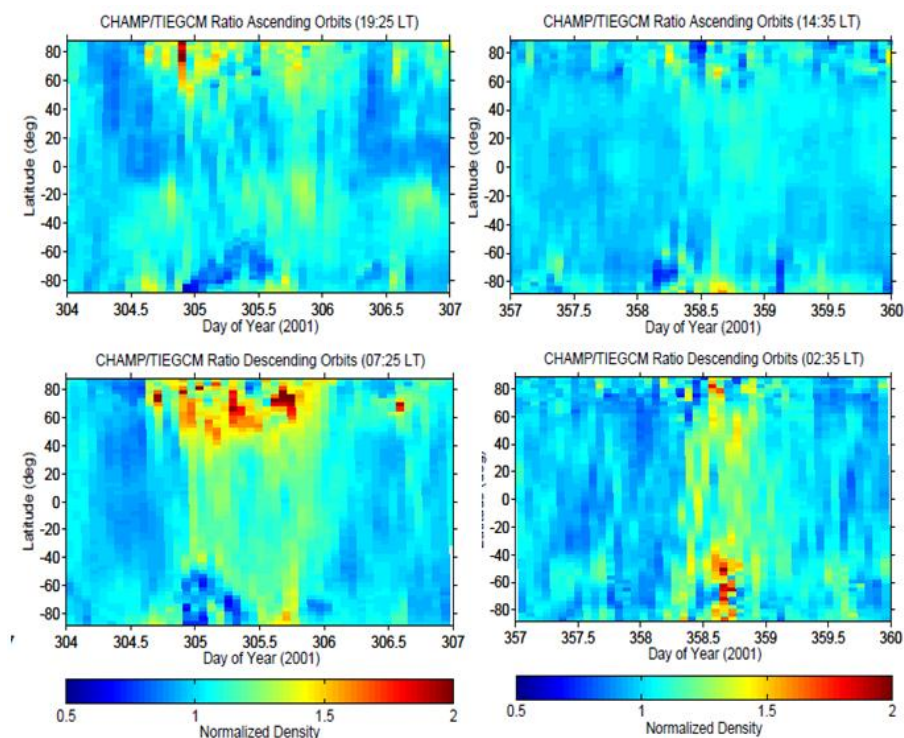


**Figure 10c: Ratio of CHAMP to TIEGCM densities for 2001 high solar flux storms**



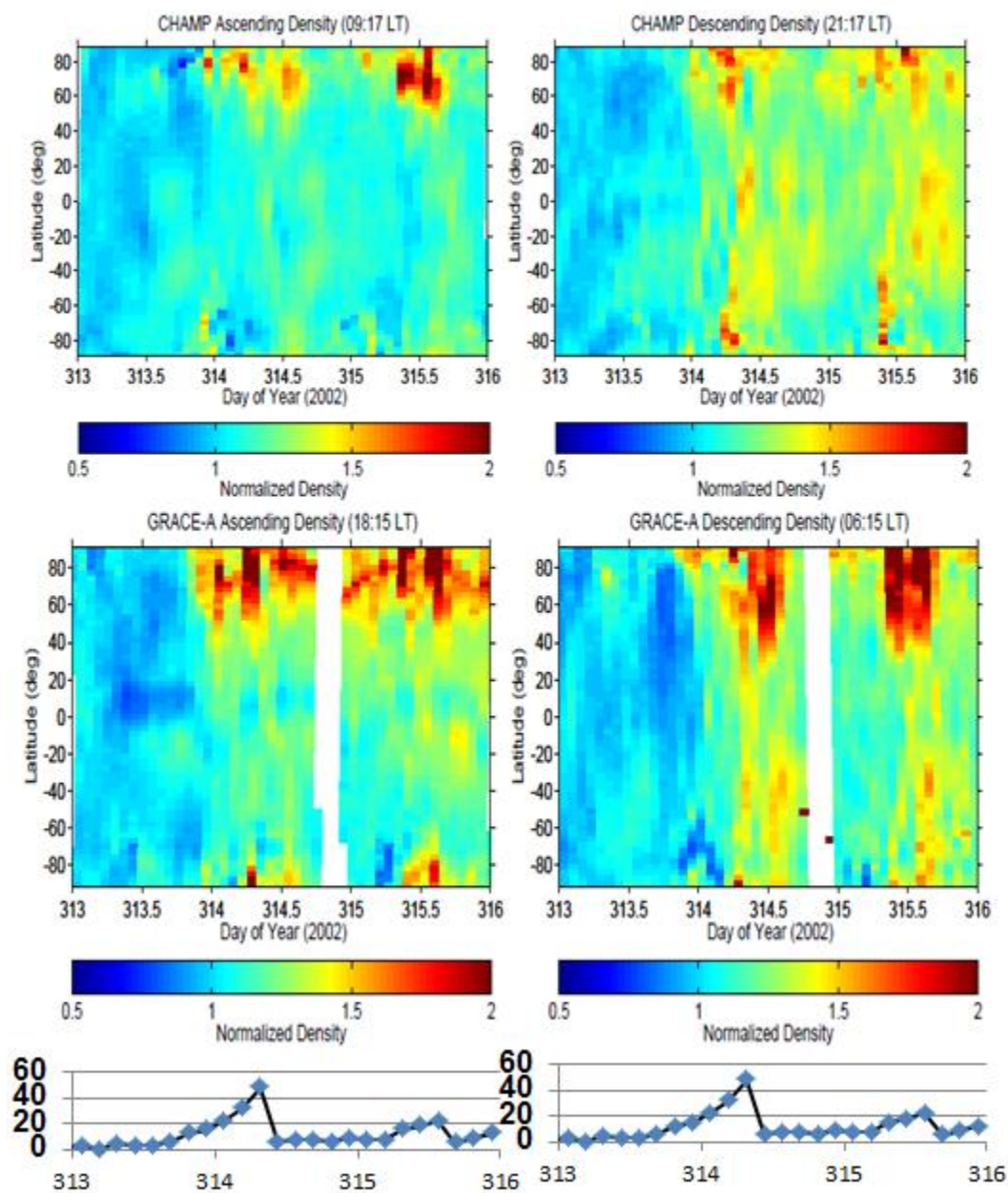


**Figure 11a: CHAMP (top panels) and GRACE (middle panels) response to same high solar flux storm. Bottom panels are ap values.**

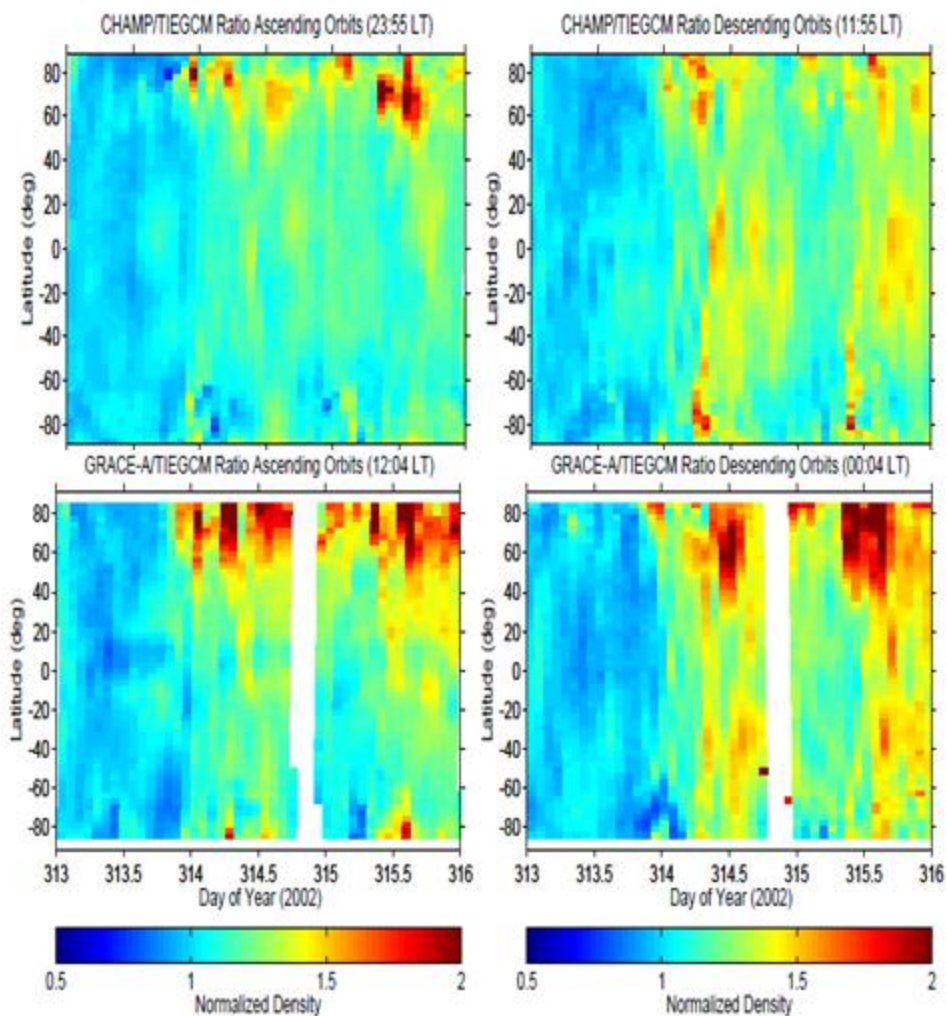


**Figure 11b: Ratio of CHAMP and GRACE to TIEGCM densities for 2002 high solar flux storm.**

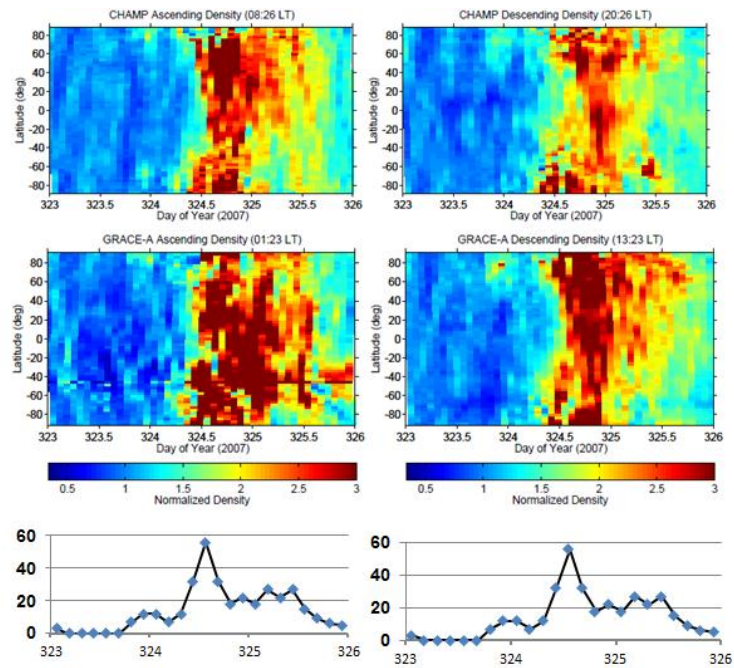


**Figure 12a: CHAMP and GRACE 2007 geomagnetic storm responses at low solar flux. Top: CHAMP data; middle: GRACE data. Bottom panels are ap values.**

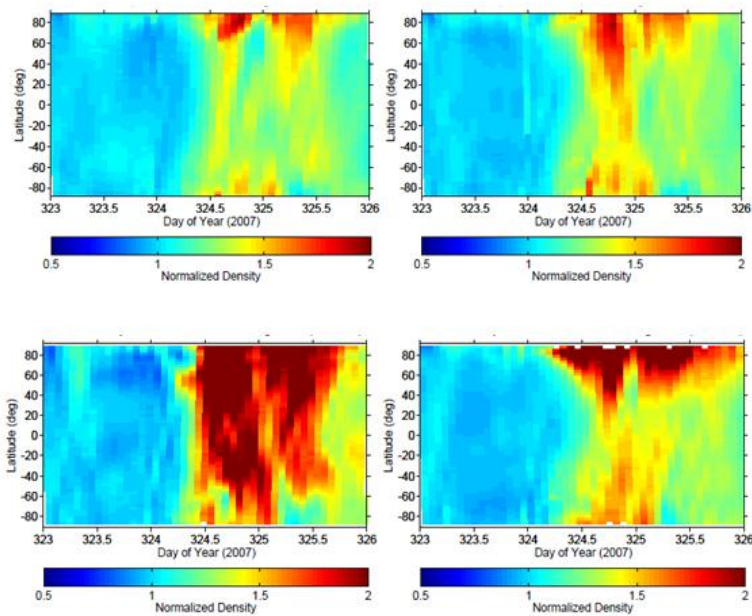


**Figure 12b: TIEGCM simulations of 2007 storm at CHAMP (top) and GRACE (bottom) altitudes.**



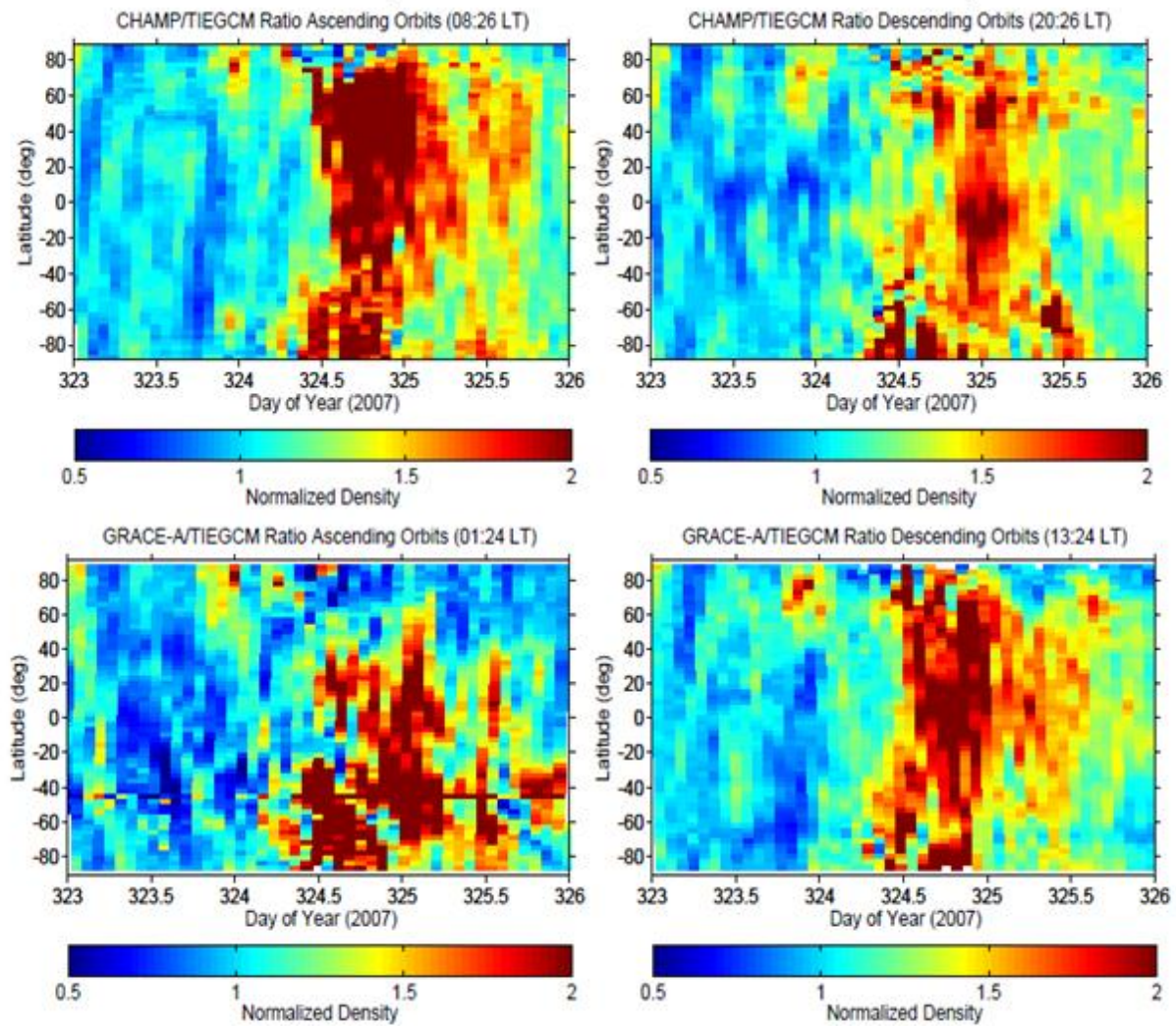


**Figure 12c: Ratio of CHAMP and GRACE to TIEGCM densities for 2007 low solar flux storm.**

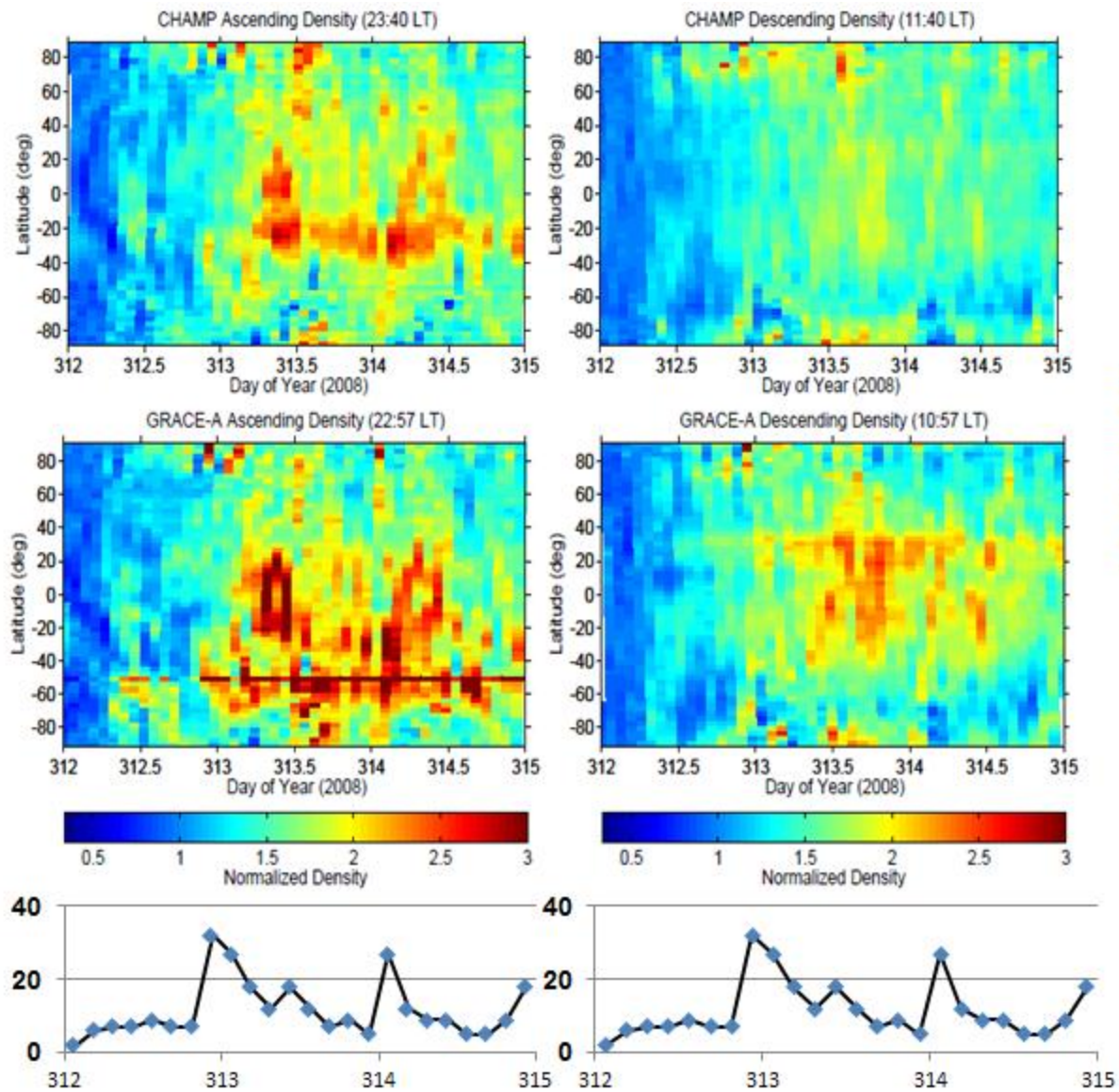


**Figure 13a: CHAMP and GRACE 2008 geomagnetic storm responses at low solar flux. Top: CHAMP data; middle: GRACE data. Bottom panels are ap values.**



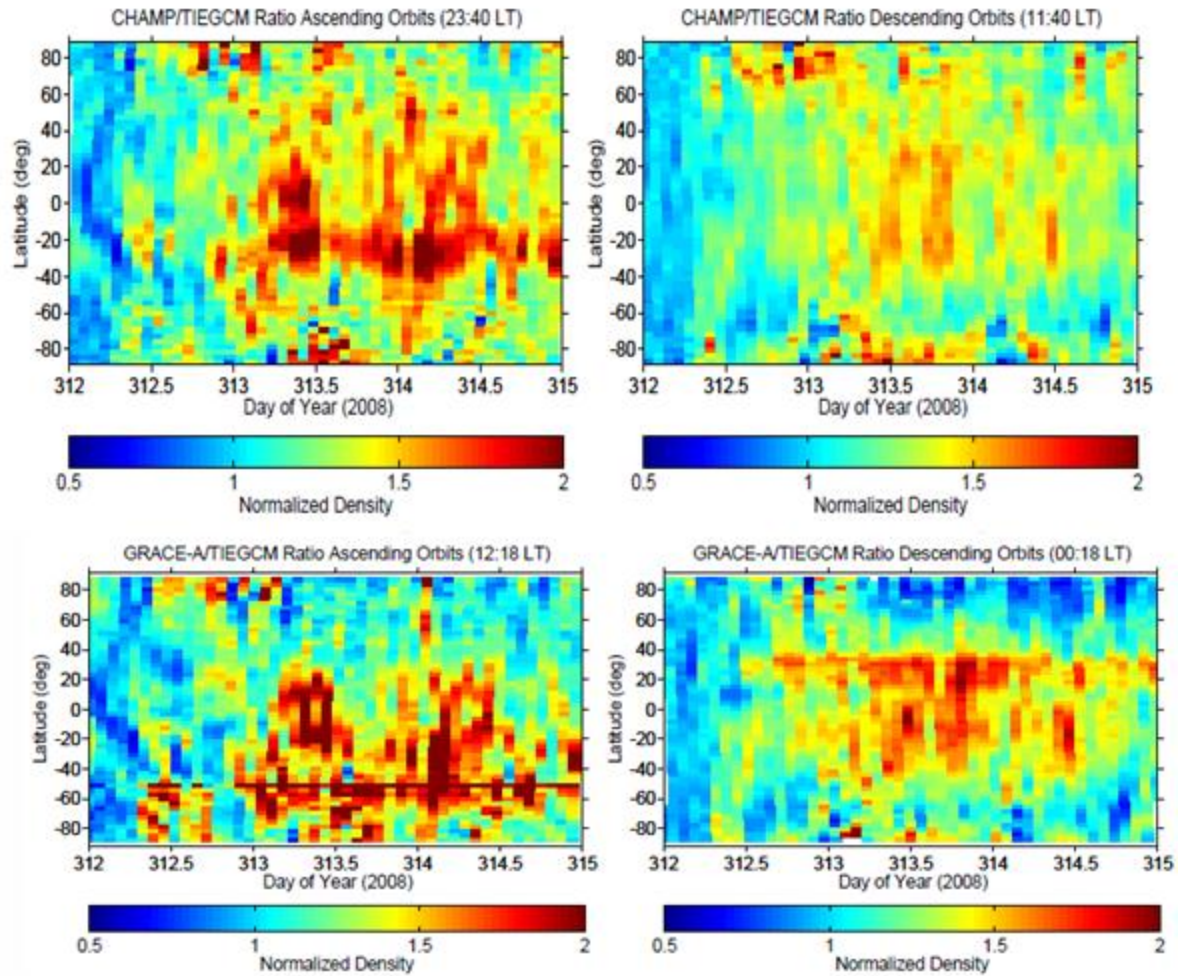


**Figure 13b: Ratio of CHAMP (top) and GRACE (bottom) to TIEGCM densities for 2008 low solar flux storm**

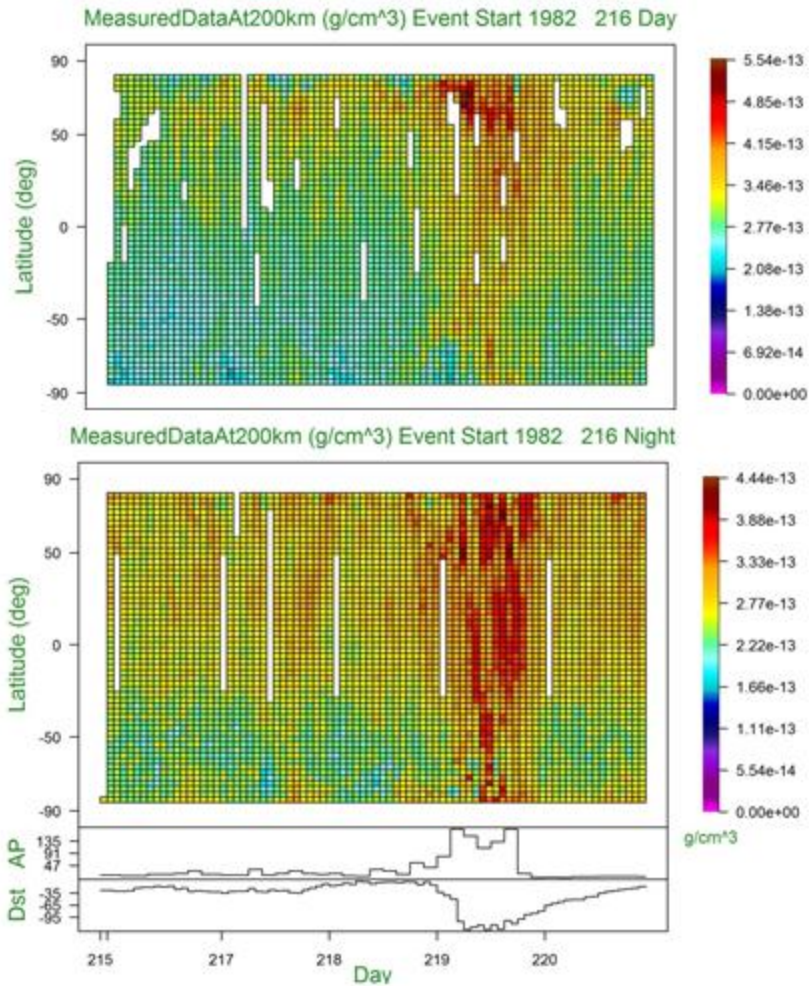


**Figure 14a: SETA-2 neutral mass density at 200 km in latitude-time coordinates for 3-8 Aug 1982 for local times near 1030 hours (top) and 2230 hours. Geomagnetic indices ap and Dst are in bottom panel.**

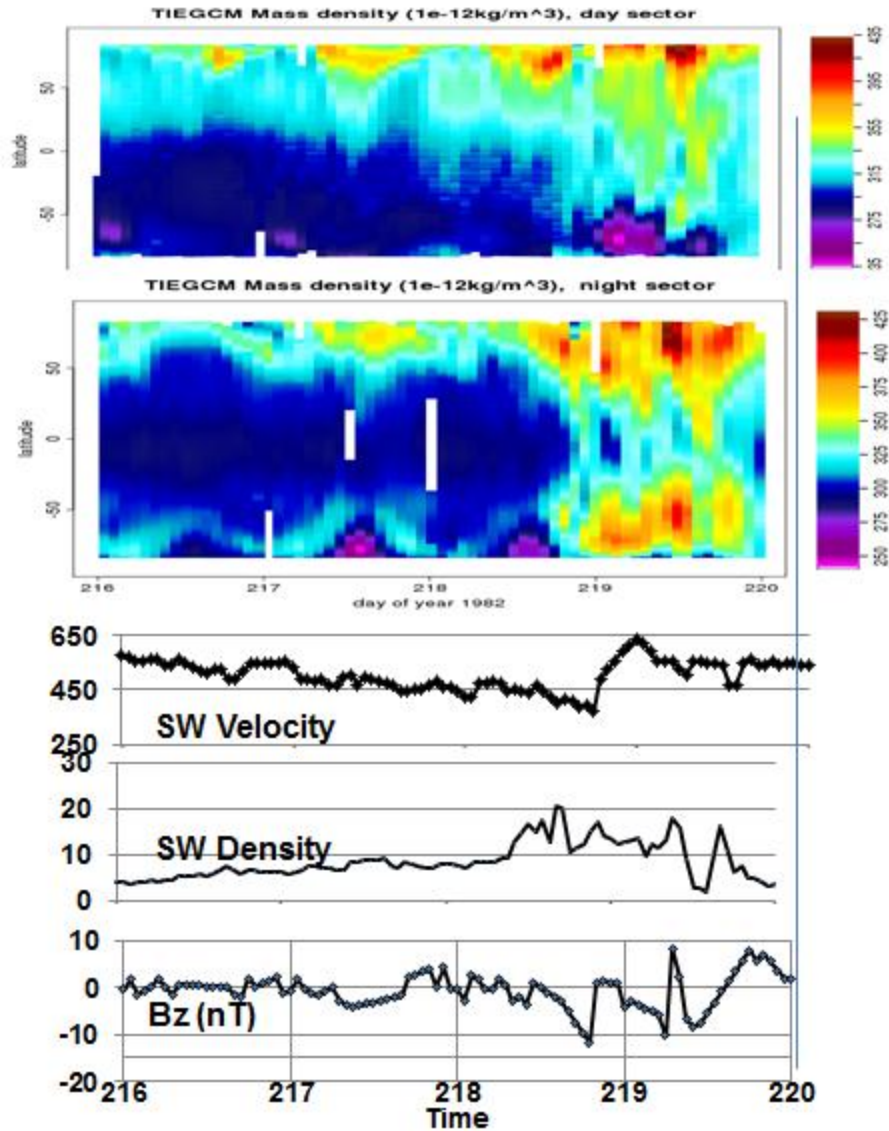


**Figure 14b: TIEGCM simulation of neutral densities normalized to 200 km at SETA-2 locations for d. 216-220 (4-8 Aug 1982). Top: Dayside (1030 LT); Middle: Nightside (2230 LT). Bottom: Solar wind inputs.**

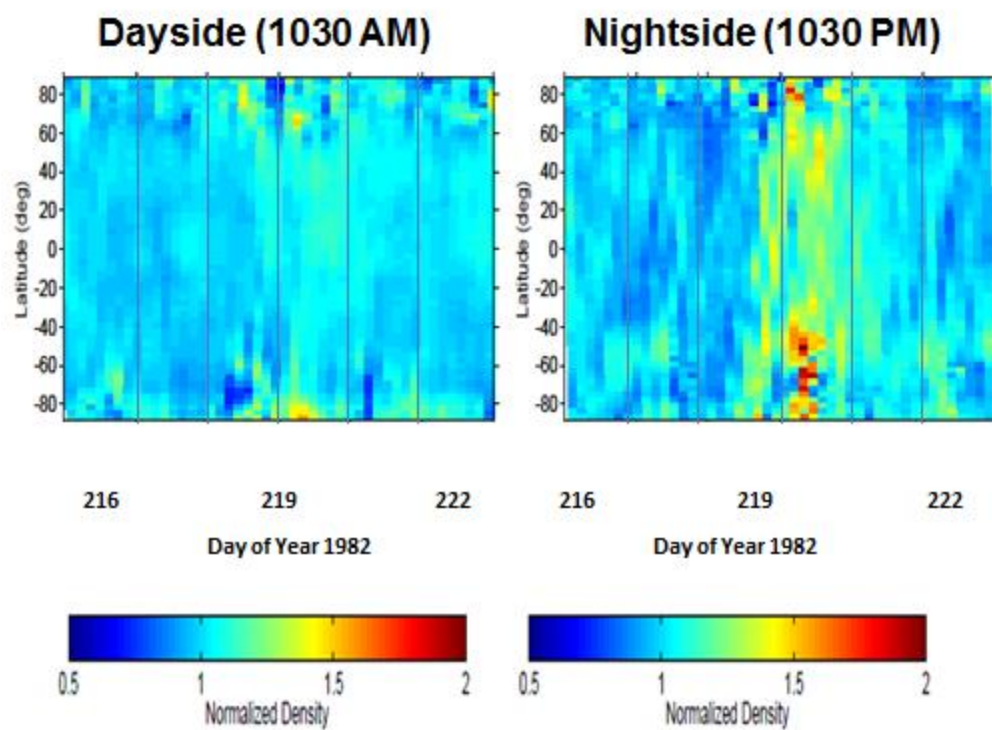


**Figure 14c: Ratio of SETA-2 to TIEGCM density for Aug 1982 storm for Local times near 1030 hours (left) and 2230 hours (right).**



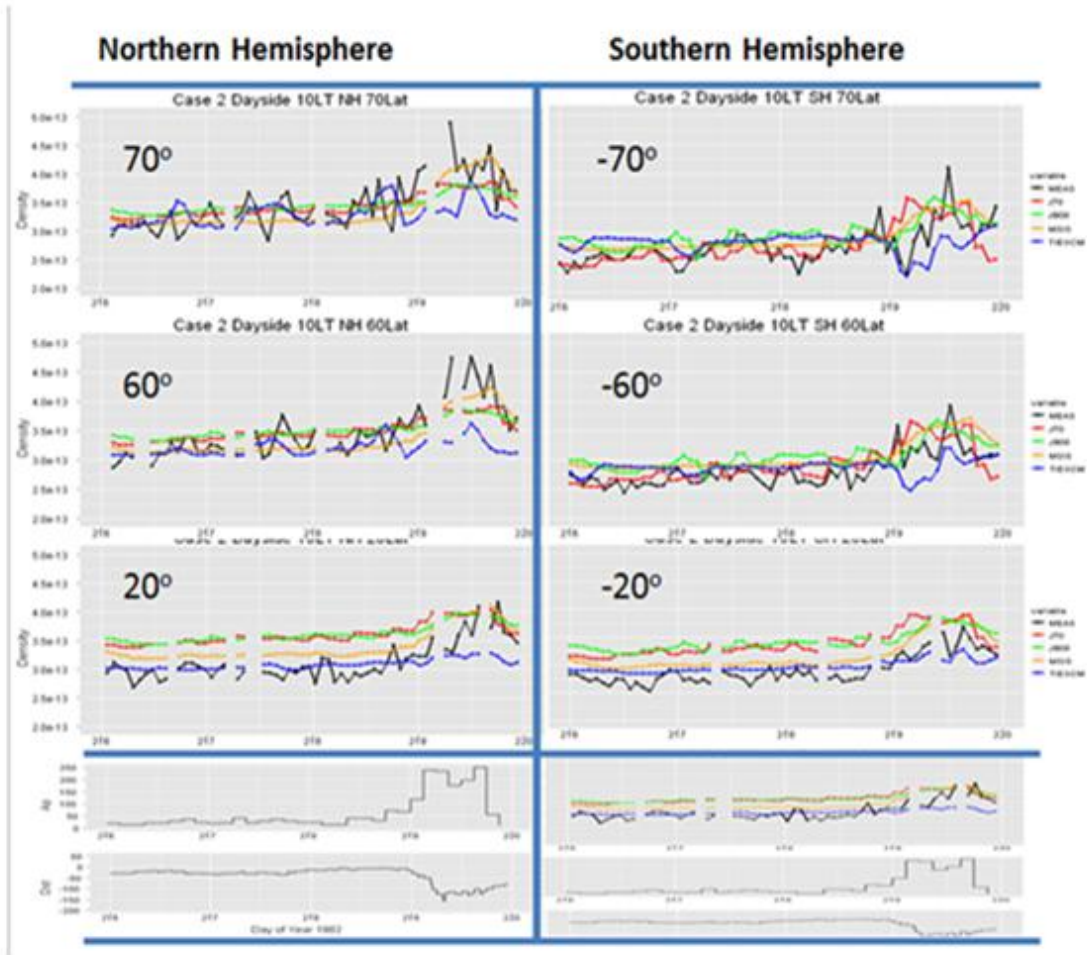


**Figure 15. Orbit-averaged density and models vs time in Aug 1982. Black: SETA-2 measurements, Red: J70 model, Green: JB08 model. Orange: NRLMSIS model and Blue: TIEGCM model.**

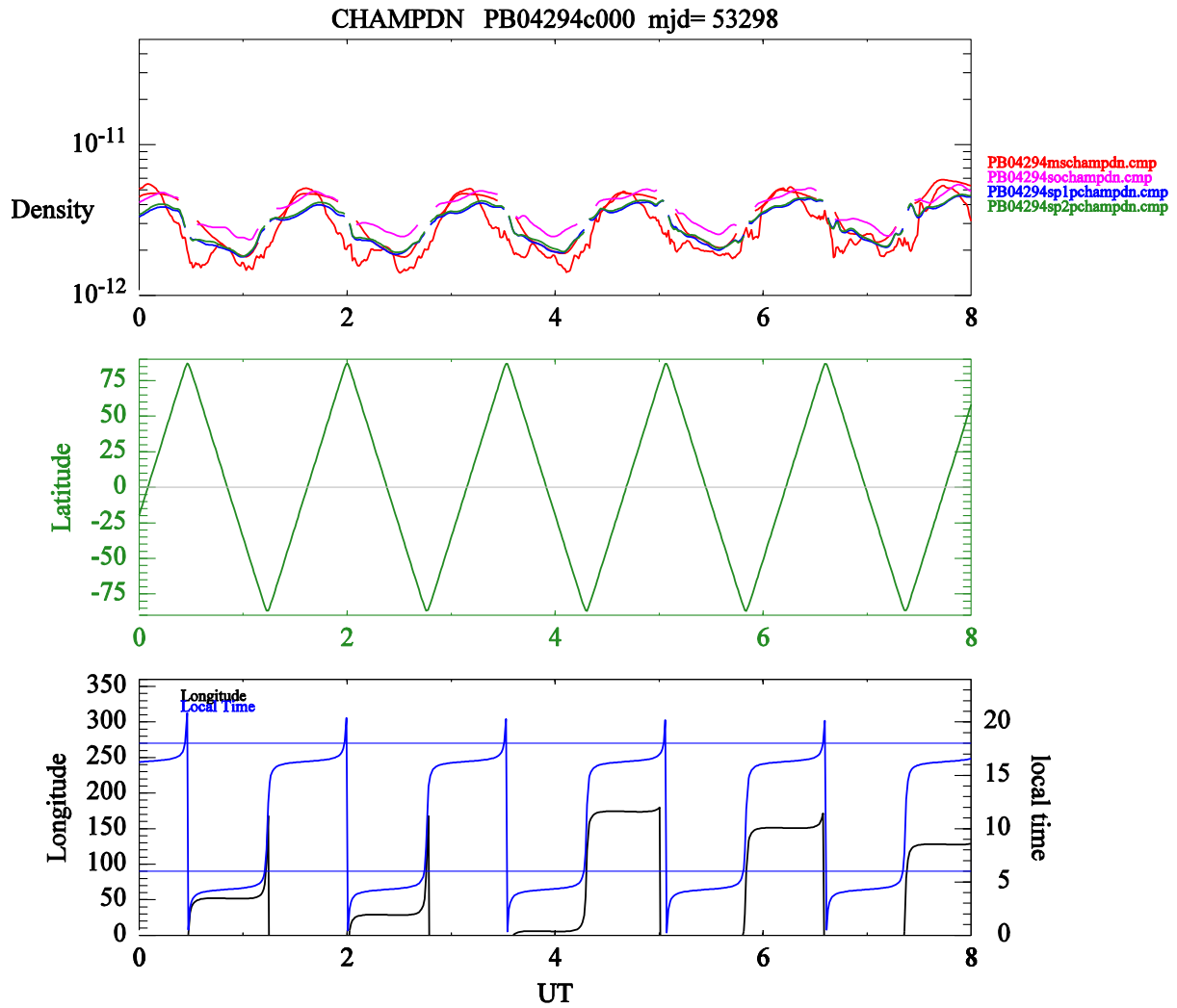


**Figure 16a: Density during part of day 294, 2004, vs unconstrained models. Top: mass density from CHAMP (red), NRLMSIS (black) and TIEGCM results using SEE EUV(pink), EUVAC (blue and green with different time resolutions of geomagnetic activity data – see text). Middle: Satellite latitude. Bottom: Satellite longitude (black) and local time (blue).**



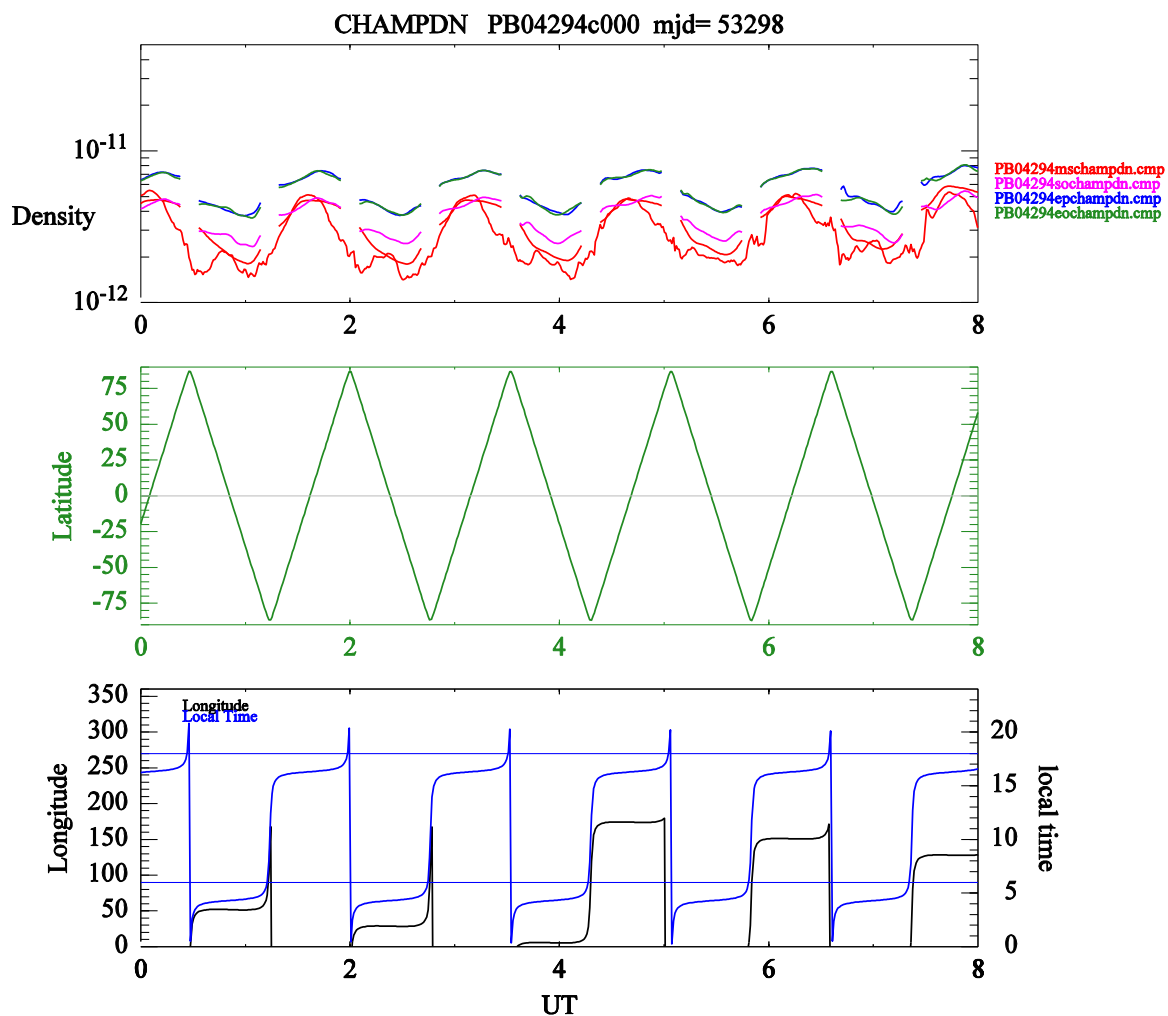


**Figure 16b:** Same as for Figure 16a but with TIEGCM runs constrained by adjusting rate factors to better match the density data. In the top panel the blue curve is the TIEGCM/SEE run with the NO cooling factor adjusted; the green curve adds a joule heating adjustment. The pink and black curves are as in Figure 16a.

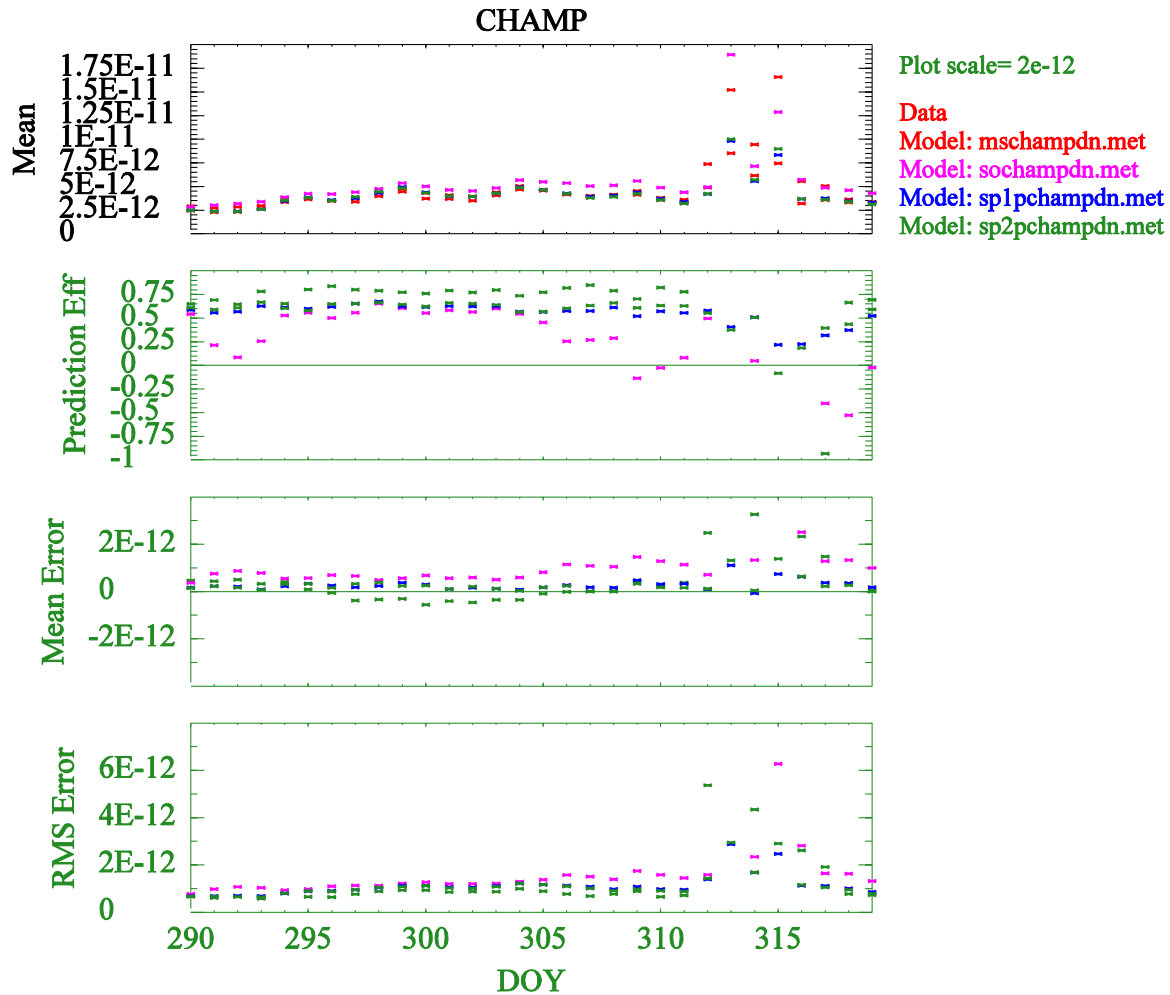


**Figure 16c: Data assimilation using variable NO cooling rate and joule heating parameters for TIEGCM Nov 2004 CHAMP data simulation. Top panel: Mean daily density for CHAMP (red); NRLMSIS (black) and TIEGCM runs (i) unconstrained (pink), (ii) with adjusted NO cooling (blue) and (iii) adjusted NO and joule heating (green). Second panel is the prediction efficiency: the observational variance minus the mean square model error, normalized by the observational variance; Third panel is the mean model error. Fourth panel is the root mean square model error.**

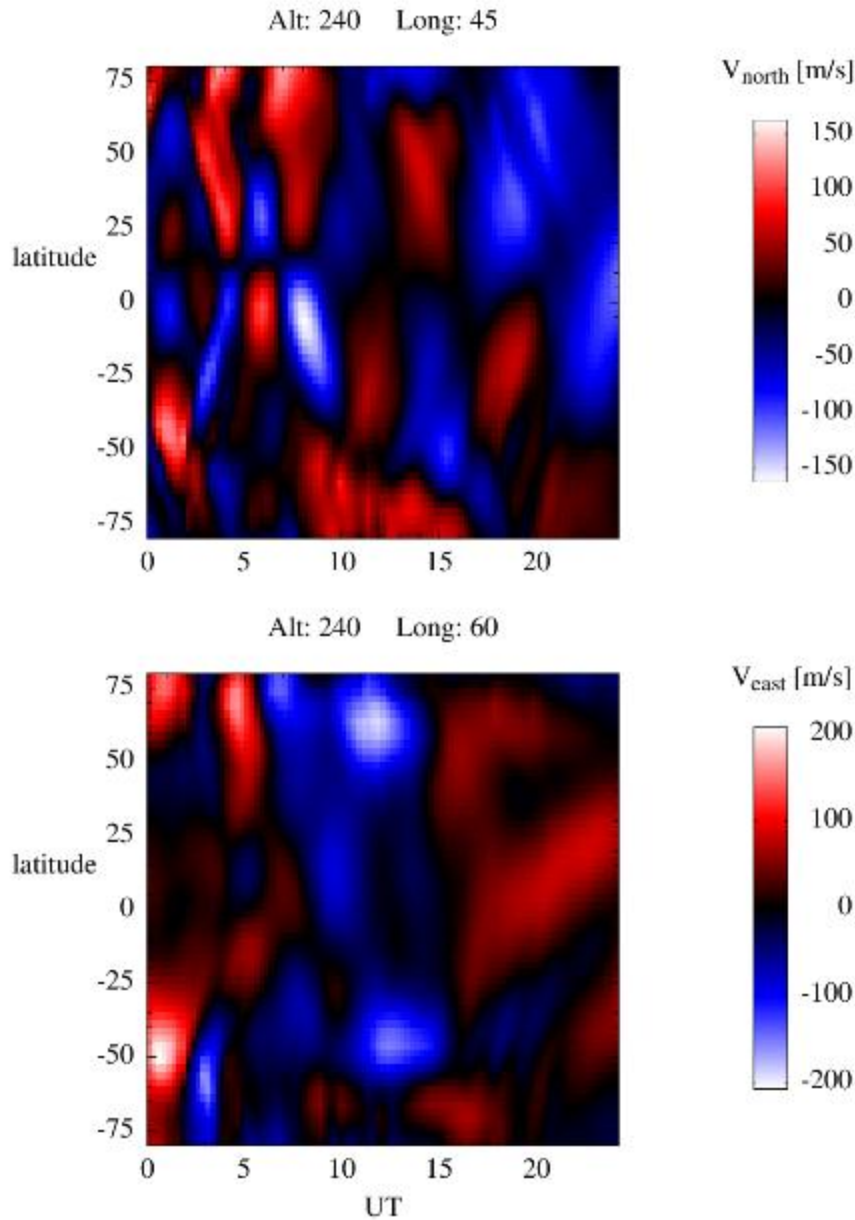


**Figure 16d: Latitude-UT difference in neutral winds at 240 km between two model runs (constrained and unconstrained) during an interval of geomagnetic activity (day 315, 2004). The top panel is the meridional wind, the bottom panel the zonal wind. The constrained model had the NO cooling factor fitted to have its densities better match the CHAMP densities.**

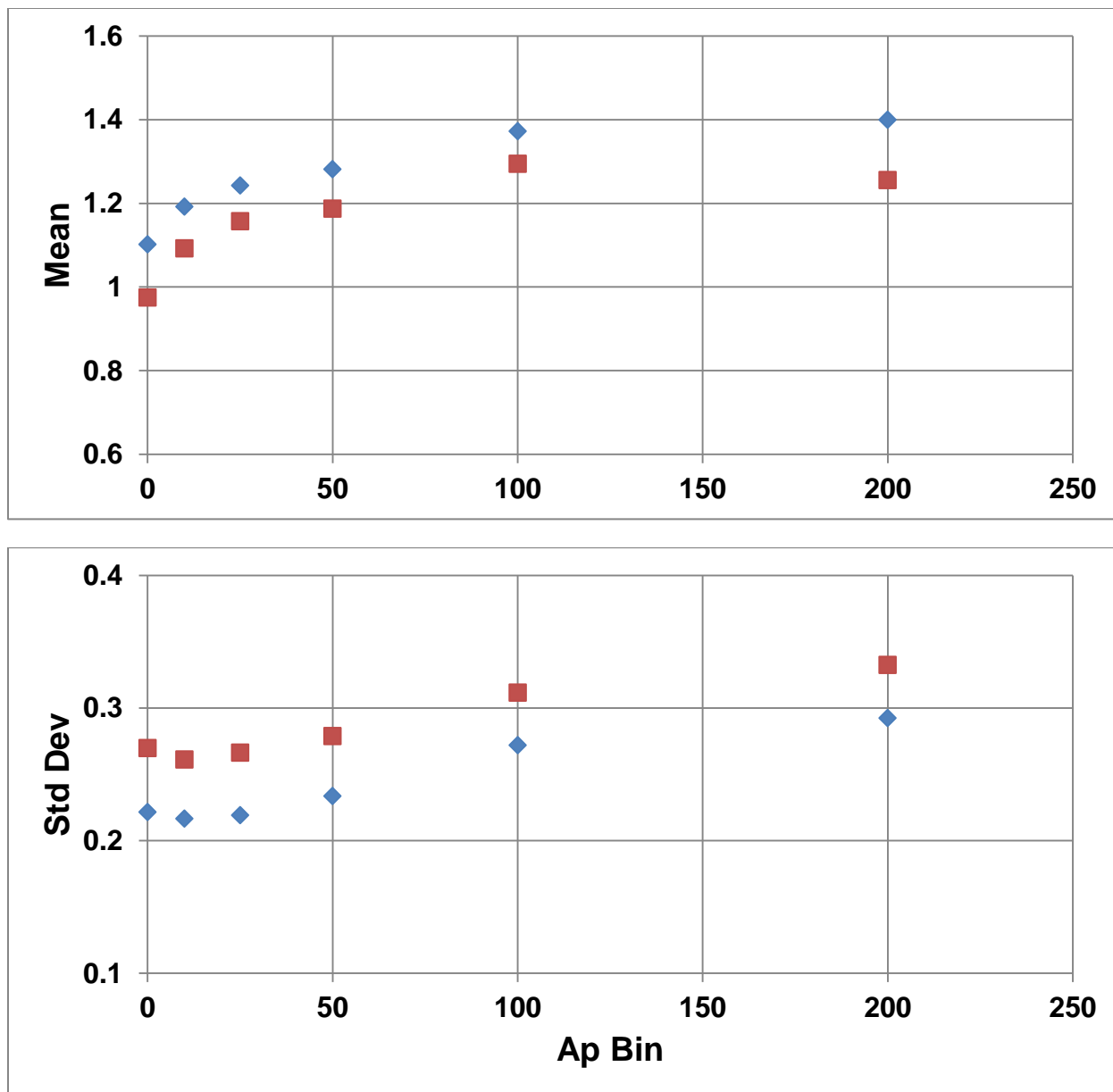


**Figure 17a: Mean (top) and standard deviations (bottom) of CHAMP/TIEGCM northern hemisphere data, in six ap bins, for day (blue) and night (red) local time bins.**

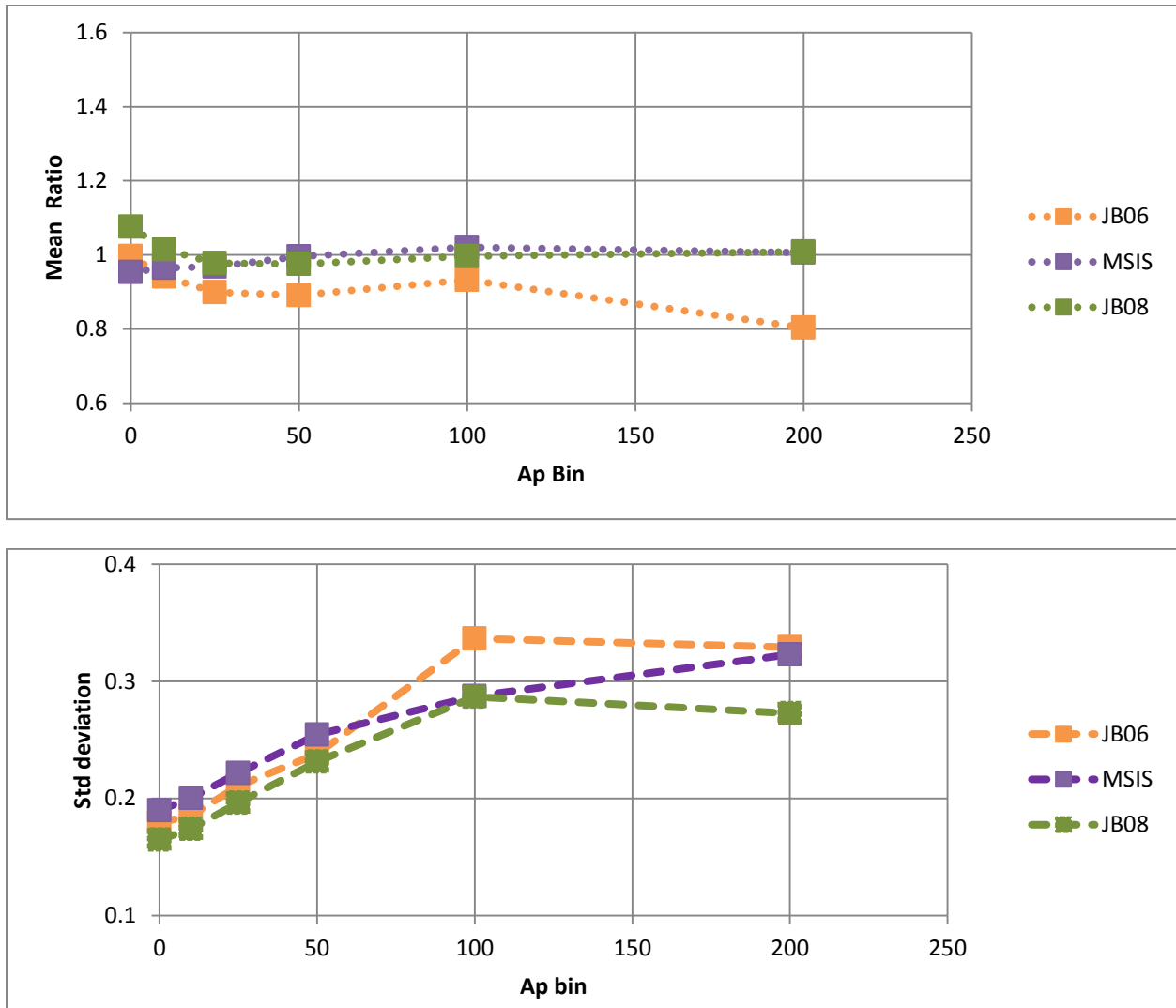


**Figure 17b: Mean (top) and standard deviations (bottom) of CHAMP/Empirical Model data (no local time or hemisphere binning)**

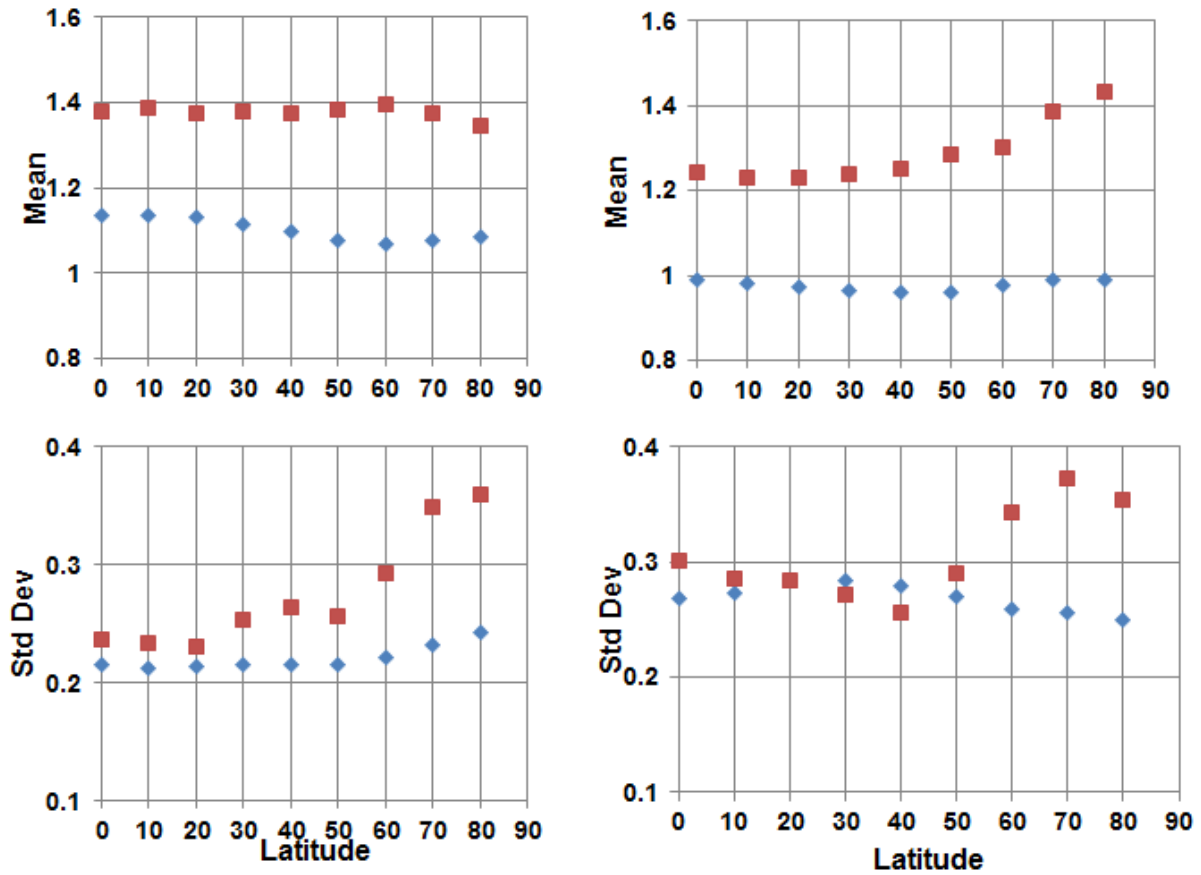


**Figure 18a: CHAMP to TIEGCM ratios vs latitude for northern hemisphere data in two ap bins, 0-10 (blue) and >100 (red). Left: daytime local times; Right nighttime local times**

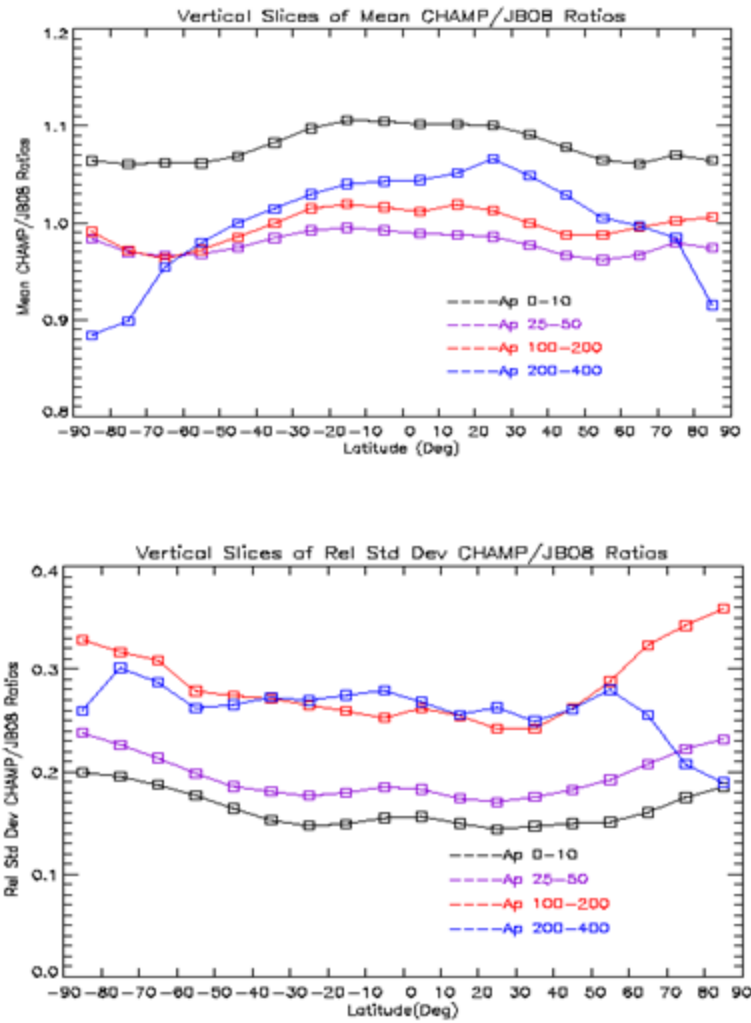


**Figure 18b: CHAMP to JB08 ratios in four ap bins. Data cover all latitudes and are for all local times. Mean values (top) and standard deviations (bottom).**

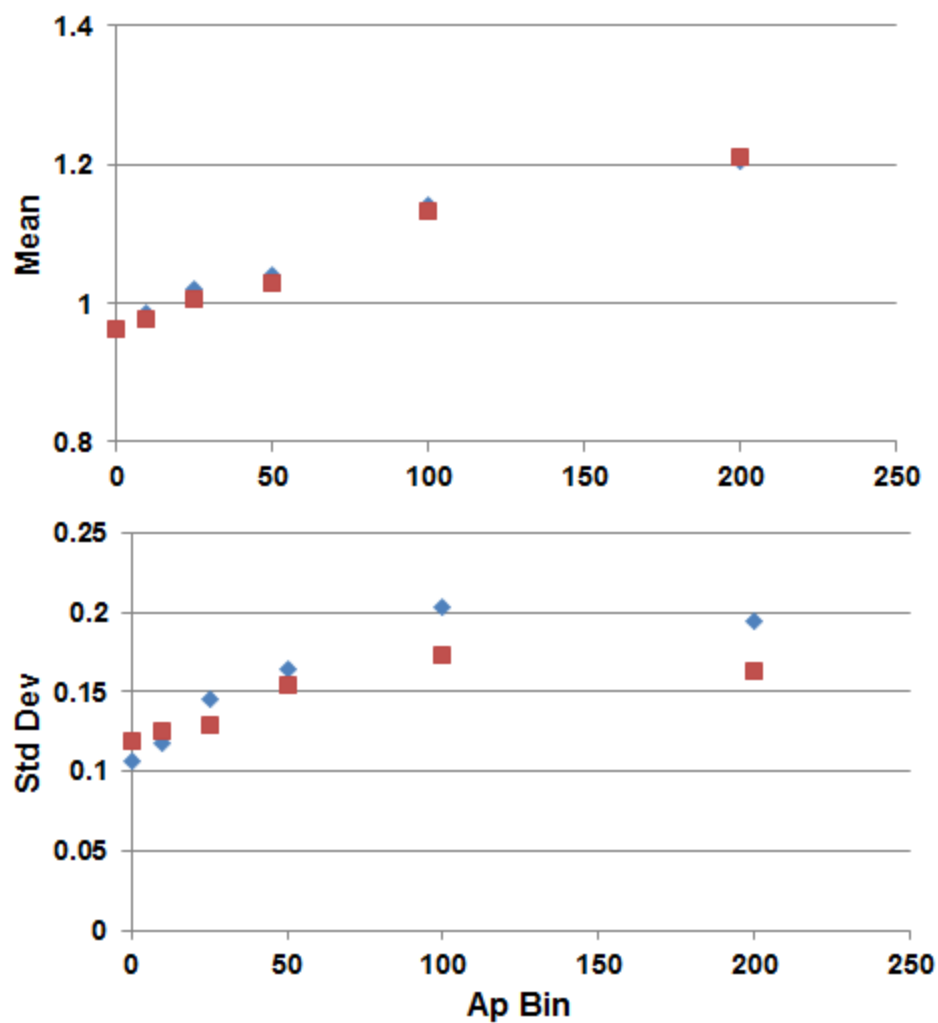


**Figure 19a: Mean (top) and standard deviations (bottom) of SETA-2/TIEGCM northern hemisphere data, in six ap bins, for day (blue) and night (red) local time bins.**



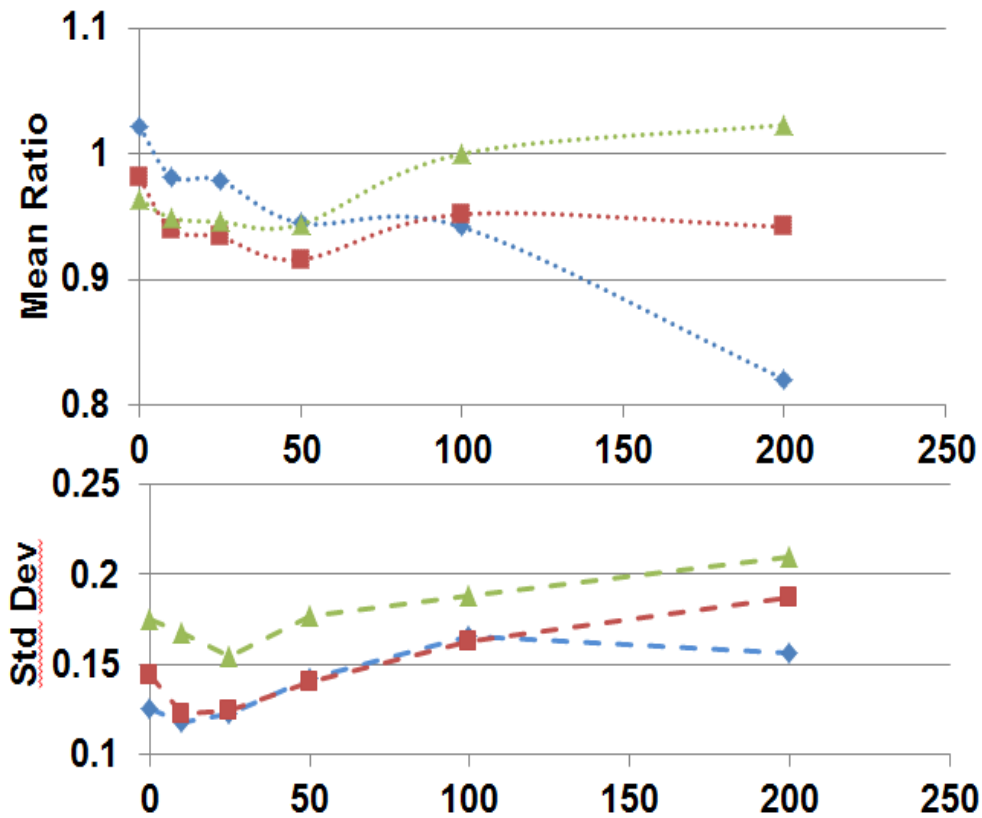
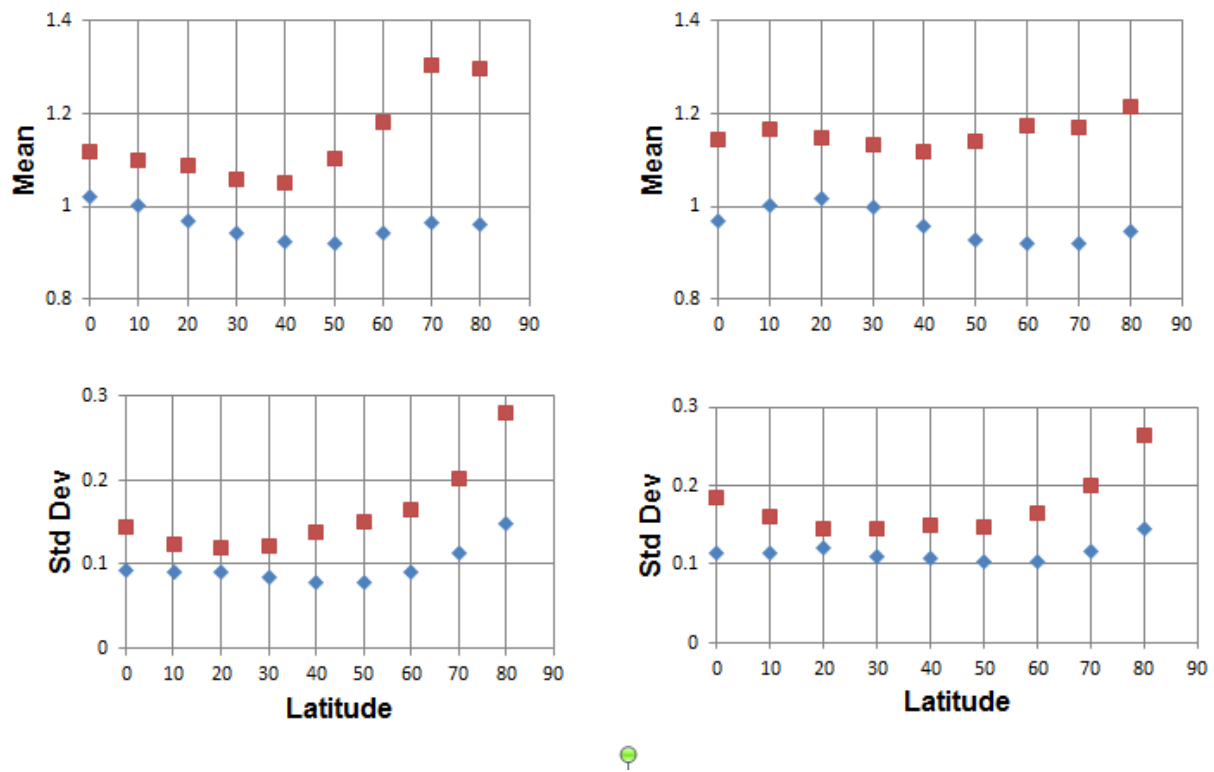


Figure 19b: Mean (top) and standard deviations (bottom) of SETA-2 to empirical models, day local times and northern hemisphere data, in six ap. Ratios of data are to: Blue: NRLMSIS, Red: J70, Green: JB08.



**Figure 20a: SETA-2 to TIEGCM ratios vs latitude for northern hemisphere data in two ap bins, 0-10 (blue) and >100 (red). Left: daytime local times; Right: nighttime local times**

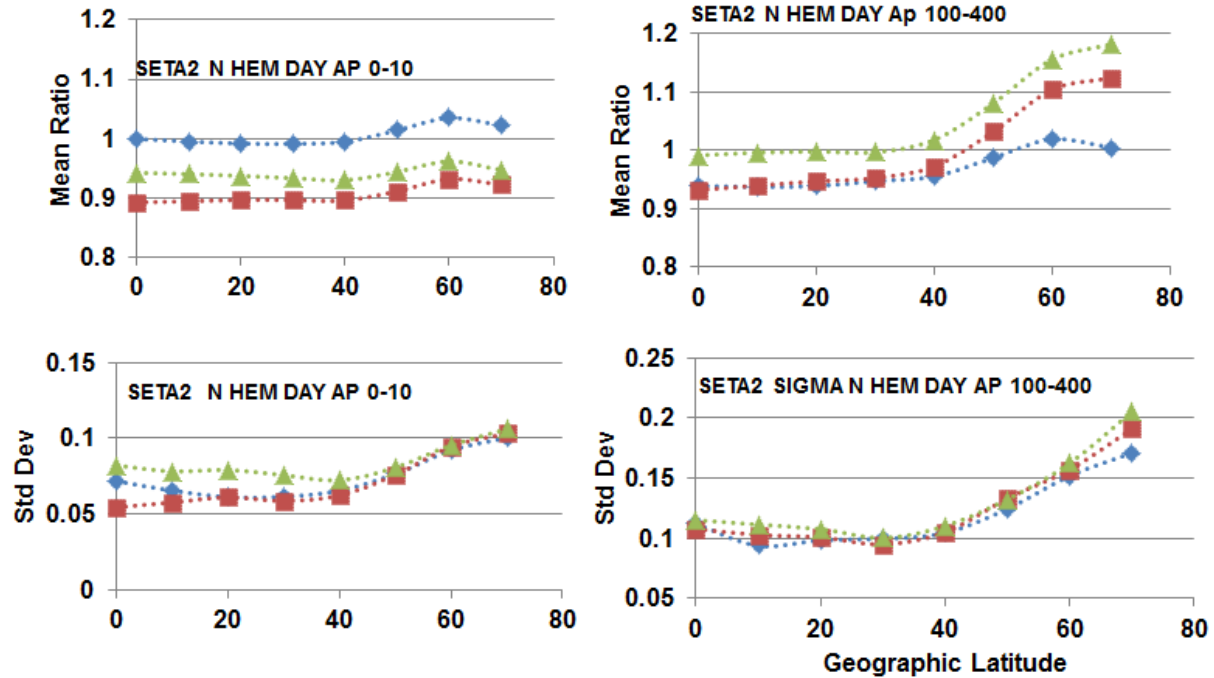


Figure 20b: Northern hemisphere dayside Seta-2 mean values (top) and standard deviations (bottom) for data-to-empirical model ratios binned by dayside (left) and nightside (right). Data are for ap 0-10 (left) and ap 100-400 (right). Ratios are of data to: Blue: NRLMSIS, Red: J70, Green: JB08.

## **DISTRIBUTION LIST**

DTIC/OCP 8725 John J. Kingman Rd, Suite 0944 Ft Belvoir, VA 22060-6218	1 cy
AFRL/RVIL Kirtland AFB, NM 87117-5776	2 cys
Official Record Copy AFRL/RVBXP/Dr. Daniel Ober	1 cy